Design and Characterization of an 8x8 Lateral Detector Array for Digital X-Ray Imaging

by

Christos Hristovski

A thesis

presented to the University of Waterloo

in fulfillment of the

thesis requirement for the degree of

Master of Applied Science

in

Electrical and Computer Engineering

Waterloo, Ontario, Canada, 2010

AUTHOR'S DECLARATION

I hereby declare that I am the sole author of this thesis. This is a true copy of the thesis, including any required final revisions, as accepted by my examiners.

I understand that my thesis may be made electronically available to the public.

Abstract

X-ray imaging has become one of the most pervasive and effective means of diagnosis in medical clinics today. As more imaging systems transition to digital modes of capture and storage, new applications of x-ray imaging, such as tomosynthesis, become feasible. These new imaging modalities have the potential to expose patients to large amounts of radiation so the necessity to use sensitive imagers that reduce dose and increase contrast is essential.

An experimental design that utilizes laterally oriented detectors and amorphous semiconductors on crystalline silicon substrates has been undertaken in this study. Emphasis on fabricating a device suitable for medical x-ray imaging is the key principle throughout the design process. This study investigates the feasibility and efficiency of a new type of x-ray imager that combines the high speed, low noise, and potential complexity of CMOS circuit design with the high responsivity, large area uniformity, and flexibility of amorphous semiconductors.

Results show that the design tradeoffs made in order to create a low cost, high fill factor, and high speed imager are realistic. The device exhibits good responsively to optical light, possesses a sufficient capacitive well, and maintains CMOS characteristics. This study demonstrates that with sufficient optimization it may be possible to design and deploy real time x-ray system on chip imagers similar to those used in optical imaging.

Acknowledgements

This work would not be possible without the guidance and trust of my supervisor, Dr Karim, who took me in as a graduate student knowing essentially nothing about me. It was this attitude and demeanor of trust that gave me the will and freedom to work in the UWSTAR group even when things got hectic and, to me, seemed unfair. I have him to thank for giving me a chance.

The rest of the UWSTAR group that contributed to this research and testing deserve shout-outs starting with Amir Goldan for the circuit design, Bahman Hadji and Dali Wu for circuit codesign, Dr Wang for a-Si deposition and guidance in testing, Dr Majid and Shiva for a-Se deposition, Nic Allec for some x-ray theory and light hearted laughs, Yuan Fang for the odd smile, and Umar Shafique for comic relief.

The professors that read my drafts and served as consultants for this thesis also deserve my thanks for working with me on such short notice and on a quick time scale. The University of Waterloo that has provided me with almost seven years of student loans, amazing facilities, and enough characters to fill out every checkbox on a personality survey should also be thanked and appreciated for never being a problem or limiting factor in the scope of my work.

I'd also like to thank Mary for being there for me when needed the most, or least, or any time she felt it. The mood swings, the wild highs, and the tremendously insightful time spent together talking about whatever came to the frontal lobes has allowed me to be creative, consolatory, and comfortable being a friend to people I may not even get along with. You've taught me to be a professional, personal, productive and never the pessimist I was when I had started university. For opening my mind I thank you.

Table of Contents

AUTHOR'S DECLARATION ii

Abstract iii

Acknowledgements iv

Table of Contents v

List of Figures viii

List of Tables xi

Chapter 1 X-Ray Imaging Theory and Applications 1

1.1 The History of Electromagnetic Radiation and X-rays 1

1.2 X-Ray Physics and Generation 4

1.2.1 X-Ray Production 5

1.2.2 X-Ray Generators 6

1.3 X-ray Image Contrast Capturing Physics and Image Generation 8

1.4 X-ray Modalities and Imaging Areas 11

1.4.1 Chest and General Radiography 11

1.4.2 Mammography 13

1.4.3 Fluoroscopy 13

1.4.4 X-Ray Computed Tomography 15

1.5 High speed X-ray imagers 16

1.6 Summary and Thesis Organization 17

Chapter 2 Detector Structures, Amorphous Photoconductors and Backplanes for Large Area Imaging 19

2.1 Large Area Imaging Systems 19

2.2 Indirect and direct detection 21

2.2.1 Indirect Conversion 22
2.2.2 Amorphous materials as Photoconductors 24
2.2.3 Material Arrangement and Properties of Amorphous Semiconductors 24
2.2.4 Stabilized Amorphous Selenium as a Photoconductor 28
2.2.5 Amorphous Silicon as a Photoconductor 33
2.2.6 Summary 35
2.3 Detector Structure 35
2.3.1 Vertical Detectors 36
2.3.2 Lateral Detectors 37
2.3.3 Detector Structure Summary 38
2.4 Detector Circuits and Analysis 38
2.4.1 Passive Pixel Sensing 39
2.4.2 Current Mode Active Pixel Sensing 42
2.4.3 Circuit Summary 45
2.5 Backplane Selection 46
2.5.1 Amorphous Silicon Thin Film Transistor Process 46
2.5.2 CMOS 0.18um Process 48
2.6 Summary 50
Chapter 3 Design of an 8x8 array 51
3.1 Process Considerations 51
3.2 Lateral Pixel Considerations 51
3.3 PPS Array Considerations 54
3.4 Issues in fabrication 58

3.5 Issues in Photoconductor Integration and Chip Handling 60
3.6 Modifications to Test Read Board 63
3.7 Summary 64
Chapter 4 Testing 66
4.1 PPS Functionality 66
4.1.1 Transistor Performance 67
4.2 Effective Quantum Efficiency 71
4.3 Transistor Noise Performance 75
4.4 Summary 75
Chapter 5 Summary and Future Research 77
5.1 Summary 77
5.2 Thesis Contributions 77
5.3 Future Recommendations and Research Paths 78
References 80

List of Figures

Figure 1 : The Electromagnetic Spectrum 2

Figure 2 : W. Röntgen First Public X-Ray Image from 1895 3

Figure 3 : Bohr Model of Tungsten Atom with Labeled Nucleus and Electron Orbitals 4

Figure 4 : X-Ray tube showing (left) rotating anode and (right) electron focal filaments(10) 7

Figure 5 : Spectrum from a Tungsten Target at various kVp showing continuous and characteristic spectrums 8

Figure 6 : X-ray interaction showing (a) Raleigh Scattering, (b) Compton Scattering, and (c) Photoelectric Effect 9

Figure 7 : General Radiography 12

Figure 8 : Mammography 13

Figure 9 : Fluoroscopy 14

Figure 10 : Computed Tomography 15

Figure 11 : Basic digital imaging system (15) 20

Figure 12 : Imager System Components 20

Figure 13 : Direct conversion (left) vs indirect conversion (right) 21

Figure 14 : SEM of CsI rods(20) 22

Figure 15 : Output spectrum of doped CsI:Ti scintillator (19) 23

Figure 16 : Diagram of (a) crystalline solid and resultant density of states for (b) insulators, (c) semiconductors, and (d) conductors. The zero crossing on the Y axis denotes the Fermi level. 25

Figure 17 : Diagram of (a) amorphous coordination and (b) amorphous density of states. The zero crossing on the Y axis denotes the Fermi level. 27

Figure 18 : a-Se Deposition 29

Figure 19 : a-Se absorption coefficient data (30) 31

Figure 20 : PECVD chamber used for the fabrication of a-Si:H 33
Figure 21 : a-Si absorption coefficient data (35) 35
Figure 22 : Comparison of (a) basic MSM and (b) enhanced MSM vertical detectors 36
Figure 23 : Comparison of lateral detectors for (a) basic and (b) enhanced pixels 37
Figure 24 : Basic Passive Pixel Sensor (PPS) Circuit 39
Figure 25 : Current Mode Active Pixel Circuit Schematic 43
Figure 26 : Typical Inverted Staggered TFT Process 47
Figure 27 : Example of (a) high resolution array and (b) pixel binned array 52
Figure 28 : Enhanced CMOS micrograph of lateral electrodes in a pixel 53
Figure 29 : Medici E-Field Simulations for Lateral Pixel Electrodes 54
Figure 30 : Original PPS Readout Array Electronics (36) 54
Figure 31 : (left) Micrograph and (right) diagram of pixel routing and capacitor design 55
Figure 32 : 8x8 Array arrangment with internal pixel routing 56
Figure 33 : Micrograph of final 8x8 array chip with bondpads 57
Figure 34 : Optical Microscope Zoom of Active Pixel Area 59
Figure 35 : (left) SEM and (right) Optical image of array electrode peeling 60
Figure 36 : (left) Amorphous vs (right) Crystallized 2um Layer of a-Se 61
Figure 37 : Array Coated in ~500nm of a-Si:H Showing Non-uniform Deposition 63
Figure 38 : DIP Adapter for Modified Readout Circuit 64
Figure 39 : Silver Paste Shorted PPS Array 66
Figure 40 : HP 4156 Parameter Analyzer 68
Figure 41 : Ids vs Vds for various Vgs of PPS Transistor 69
Figure 42 : Ids vs Vgs for Various Vds of PPS Transistor 70

Figure 43 : EQE Setup 72

Figure 44 : EQE of a-Se Detector 73

Figure 45 : EQE of a-Si:H Detector 74

List of Tables

Table 1 : Electron Binding Energies for Specific Elements and Associated Orbitals (7) 6

Table 2 : Specifications for Digital X-Ray Imaging Systems(13) 17

Table 3 : Mobility, Lifetime, and Range of a-Se and a-Si Carriers 32

Table 4 : Comparison of Vertical and Horizontal detector structures 38

Table 5 : Comparison of Pixel Architectures for Real Time Imaging 45

Table 6 : Comparison of 0.18um CMOS and a-Si TFT MOSFET parameters 48

Table 7 : Comparison of Substrate Technologies 49

Table 8 : Final Array Properties 65

Table 9 : Summary of Results for CMOS Lateral Imagers 76

Chapter 1
X-Ray Imaging Theory and Applications

This chapter details the physical phenomena of x-rays and their uses. It starts with a detailed description of the properties of electro-magnetic radiation (EMR) that are commonly classified as x-rays. Then, common modern methods of x-ray generation are described along with the resultant properties of the x-rays. The properties of different x-ray radiation then determine their applicability to different types of radiography, which is the detection and interpretation of x-ray radiation. X-ray imaging modalities, or the different modes of uses x-ray imaging, are discussed in addition to the areas of medical imaging that this thesis will cover. Metrics and requirements having to do with each of these x-ray imaging areas are established which determine the market segments available for real time x-ray digital imaging systems. Finally, an outline of the goal and scope of this thesis are given in addition to the design criteria used, characterization tools developed and used, and the experience gained in order to design more efficient and effective real time x-ray imagers.

1.1 The History of Electromagnetic Radiation and X-rays

In 1861 James Maxwell published "On Physical Lines of Force" [1] which set out to define, quantify, and establish a mathematical basis for the forces observed that were caused by negative and positive charges moving through space. In this first of four major papers looking to formulate equations that described the movement of charges Maxwell noted that light, when moving in a free medium such as air, not only propagated at a fixed speed but also that light consisted of both magnetic and electrical transverse oscillations. Using this assumption Maxwell was able to define the property of wavelength, λ, and periodic time or frequency, v as:

$$\lambda = \frac{c}{v} \tag{1.1}$$

It was not until Maxwell's third paper, "A Dynamic Theory of the Electromagnetic Field" [2], however, that this relationship was extended to all electromagnetic waves, of which visible light Maxwell was convinced was just one narrow band of frequencies. In addition to new modeling of EM waves Maxwell posited that the energy of a volume of light was inversely proportional to the wavelength which would now represent a broad spectrum of potential energetic radiation that was predicted by the math although never observed. He posited that waves of sufficiently high energy should be able to interact with matter with a type of mechanical force. Although his exact numerical formula was quantitatively wrong,

due to the fact that the quantum nature of photons and light would not be discovered for another thirty years, it was qualitatively right in that he predicted that the energy of an electromagnetic wave was inversely proportional to the wavelength or linearly proportional to the frequency, which is now known to be given by the relationship:

$$E = h * v \tag{1.2}$$

Where h is Plank's constant, equal to 4.13566733×10^{15} eV·s, v is the frequency in Hertz, and E represents the energy in eV. Using equations 1.1 and 1.2 Figure 1 can be constructed to map out the entire electromagnetic spectrum. The spectrum is commonly broken up and referred to in terms of bands that roughly correspond to how the EM fdwaves interact with matter. As the frequency of an EM waves increases it possesses more energy and gains the ability to change the electrical composition, or ionize, atoms by interacting and altering the electron distribution that surrounds the atom with specific types of high energy exchange mechanisms. Radiation that can remove an electron from a host atom is referred to as ionizing radiation and starts with the ultraviolet band, including the x-ray and gamma radiation band names as well, encompassing roughly any EM wave that possesses more than 5eV.

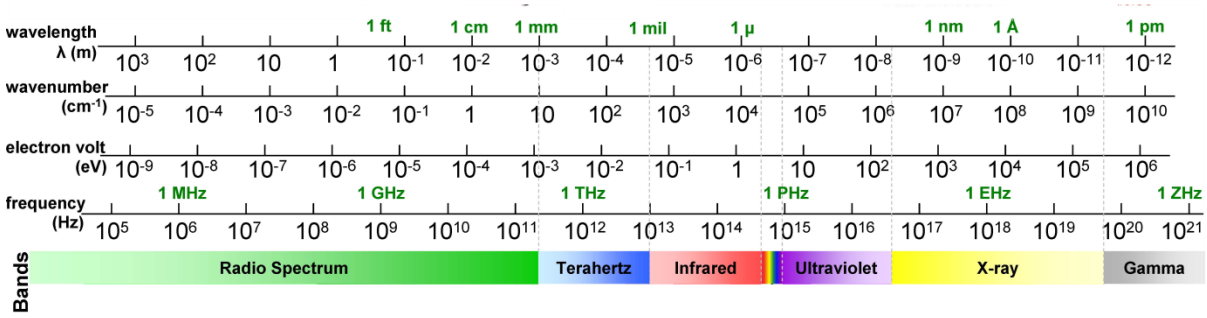

Figure 1 : The Electromagnetic Spectrum

Exploring this area of high energy radiation did not advance significantly after Maxwell's papers until Wilhelm Röntgen observed fluorescence in a nearby crystal when operating a high energy electronic vacuum tube [3]. Almost immediately, even without understanding the physical origins of the rays he was experimenting with, he was able to deduce properties of the x-rays, a term he coined, and found that they had the ability to pass through certain objects with relative transparencies that depended on the type of

material the object was made of. Soon, he and many other scientists were using x-rays for non-invasive diagnosis and this was the largest reason he was awarded the Nobel Prize for Physics in 1901, the first prize ever awarded, for his discovery. Figure 2 shows the picture Röntgen sent to a colleague in order to demonstrate his initial findings.

Figure 2 : W. Röntgen First Public X-Ray Image from 1895 [3]

An entirely new field, coined radiography, now sprung up that offered the amazing capability of internal diagnoses and non-invasive observations of the human body in a cost effective manner. Within ten years of Röntgen's discovery there were medical clinics offering the ability to pinpoint objects within the human body or diagnose potential issues with a patient's organs or bones. General Electric had produced a semi-portable x-ray image closet, textbooks had been written on how to optimize image quality, and x-rays were being used for experiments and studies without anybody understanding what was responsible for the rays and how they were interacting with matter. [4]

For more than one hundred years X-ray imaging technology has been one of the most widely used medical diagnostic and experimental information techniques in hospitals, laboratories, and observatories in the world. X-ray images have been used to demonstrate the double helix nature of DNA [5] and other proteins, for security scanners, mass spectroscopy, crystallography, and even for space based imagery [6], 3D-reconstruction, structure analysis, and modeling. The advance in the usage, applications, and interpretations of x-ray radiation has always been tied to the technology capable of generating and

capturing x-rays. As both aspects, the production and detection aspects of x-rays become more precise new applications can always be found and older ones can be made safer or less invasive.

1.2 X-Ray Physics and Generation

Modern x-ray generation is the result of the rapid evolution of more than a hundred years of trial, experiment, and quantum physics. In order to fully understand limitations and constraints that are inherent to x-ray imaging it is important to understand where x-rays come from and how they can interact with matter.

X-rays derive their energy from a moving electron's direct interactions with an atom. An atom is the basic unit of matter and consists of a positively charged nucleus and surrounding negatively charged electrons which are arranged around the atom. The arrangement of the electrons around the atom adhere to electrostatic attraction and repulsion forces that form well quantized arrangements around the nucleus in a stable manner. To simplify the orbital arrangements typically a Bohr model of the atom is used that shows the levels of electrons that are electrically bound to the electron as shown in Figure 3.

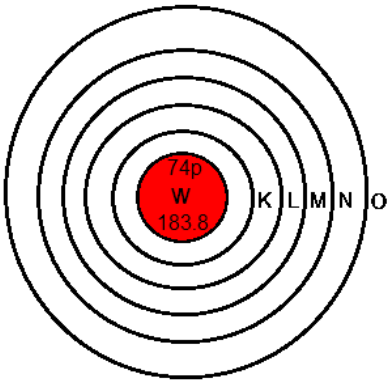

Figure 3 : Bohr Model of Tungsten Atom with Labeled Nucleus and Electron Orbitals

Electrons are classified in terms of orbital energies by the letters used to classify the orbits and electrons that are further out in the diagram represent energy orbitals that possess less electrostatic attraction to the atom. In Figure 3 the red nucleus represents a positively charged nucleus that is most strongly attracted to the K shell electrons and least bound to the O shell electrons.

1.2.1 X-Ray Production

When a high speed electron, with energies between 100eV to 100keV for the topic related to this thesis, passes near an atom there are three main ways in which the moving electron can react. The first involves elastic scattering in which the kinetic energy of the electron is reduced without radiation when the momentum is transferred to the atom in vibrational form. This is the most common high energy interaction and is responsible for most of the heat generated in x-ray tubes.

The second type of interaction is known as “bremsstrahlung” radiation, or literally braking rays. In this interaction the mobile electron gets significantly close to the atom nucleus and is induced by the atom to change its direction via electrostatic, or Coulombic, forces. Once the electron changes directions it emits a photon to balance the change of momentum. The energy of the emitted photon is directly proportional to the change in momentum that the electron experiences so the closer an electron passes to the nucleus the higher energy a photon will be emitted with a direct collision and full stop of the electron corresponding to the highest energy x-ray possible being emitted. As the incident electron interacts with other atoms the amount of kinetic energy available for this radiation decreases which results in lower amounts of radiation being emitted at higher energies. This is why the maximum x-ray spectrum occurs at the peak of the applied voltage that accelerates the electron.

The third and final way an electron can interact with an atom to produce x-rays is referred to as characteristic ionization. In this scenario the high energy electron physically collides with an electron in one of the orbitals of the atom. This collision transfers energy of the incoming electron to that of the electron of the atom. The atom’s electron is energized so that it either is totally removed from the atom or is elevated to a higher energy state within the atom. In order to relax and return the atom to a ground, or unenergized, state an electron from a higher energy orbital will drop down to fill the vacancy created by the energized electron and simultaneously emit a photon to compensate for the change in energy. The energy of the photon emitted is exactly the difference between the energy of the vacant atom orbital that is being filled minus the electron’s current orbital binding energy. This radiation, therefore, will be related to the binding energies of the atom used in x-ray production; specifically important are the K orbital electron energies which comprise the inner electron orbitals of the atom. Table 1 shows binding energies for common materials used in x-ray production and for other elements related to medical imaging. Notice that higher binding energies are present in atoms with higher atomic numbers and the low binding energies are present in organic material.

Table 1 : Electron Binding Energies for Specific Elements and Associated Orbitals [7]

	Element Binding Energy (eV)					
Orbital	Hydrogen	Carbon	Oxygen	Molybdenum	Rhodium	Tungsten
K	13.6	284.2	543.1	20000	23220	69.525
L	-	-	41.6	2866	3412	12100
M	-	-	-	506.3	628.1	2820
N	-	-	-	63.2	81.4	594.1
O	-	-	-	-	-	75.6

These high binding energy reactions produce the x-ray photons that will be considered for the topic of medical and scientific imaging. The next section will describe the limitations and methods of generating x-rays in modern imagers.

1.2.2 X-Ray Generators

Much like the automobile has slowly and steadily been refined but has remained fundamentally the same x-ray generators have remained functionally the same for almost a hundred years. Modern x-ray generators are designed to deliver high rates of x-ray flux while cooling the structure to deal with the large amounts of power required and heat generated by the high speed electron collisions required. The typical x-ray system consists of a voltage control unit that is capable of generating voltages in excess of 140kV and an x-ray tube that converts accelerated electrons into x-ray radiation using the mechanisms described in the previous section.

Modern x-ray tubes, an example shown in Figure 4, use a rotating anode hot cathode design. This design increases the life of an x-ray tube and helps with the regularity of emitted photons that result from the high energy exchanges that occur in x-ray production. The main product of x-ray production is heat [8], with more than 95% of the energy being used directly being converted to, and therefore lost, as heat.

The hot cathode is the component that is heated with large currents to encourage thermionic emission. Thermionic emission describes a state of electron energies where, due to high amounts of atomic vibrational energy, electrons can easily be ejected from a material when a voltage is applied to the target. This is the same principle used in incandescent bulbs to produce visible light. An x-ray tube commonly has two filaments in the cathode of two different sizes. The larger filament produces a larger amount of electrons for emission, and therefore a higher x-ray concentration, but introduces image blurring. Where fine, focused, and more controlled doses are required the smaller focal spot is used but this introduces heat and lifetime constraints on the anode target [9].

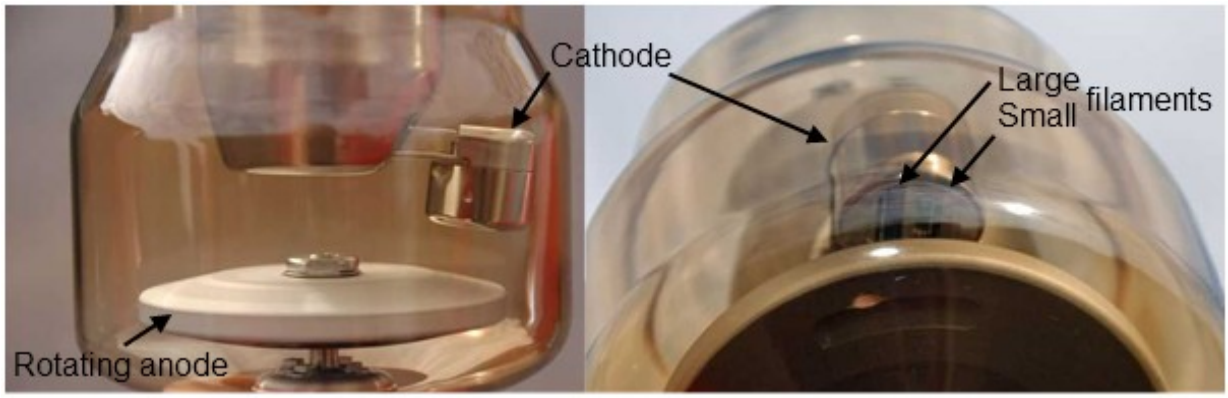

Figure 4 : X-Ray tube showing (left) rotating anode and (right) electron focal filaments [10]

Once the filament has been heated to a specified temperature the rotating anode is spun at high speeds before a large voltage is applied between the two. The magnitude and duration of the high voltage is dependent on the type of image being made which will be discussed in section 1.4. The typical x-ray spectrum produced by this method using a tungsten target can be seen in Figure 5.

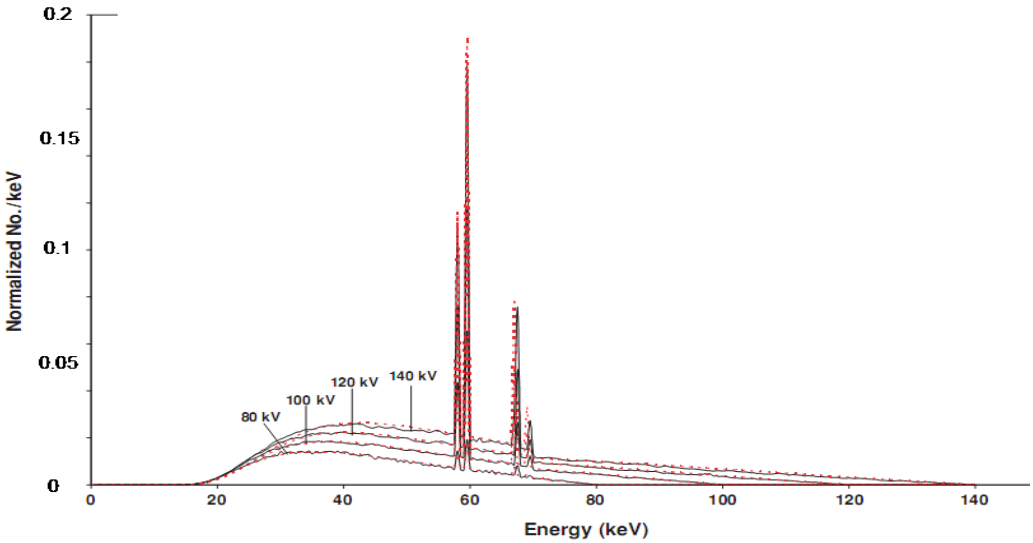

Figure 5 : Spectrum from a Tungsten Target at various kVp showing continuous and characteristic spectrums

It consists of a combination of the characteristic peaks and the continuous spectrum of the anode target minus the attenuation and filtration of the x-ray tube housing itself. In addition to this, filters can be added shift or accentuate certain x-ray energies based on their attenuation constants, as will be discussed in 1.3.

1.3 X-ray Image Contrast Capturing Physics and Image Generation

When a photon of sufficient energy passes through a physical medium there are two ways the photon can be accounted for. The photon can pass through the medium totally uninterrupted, referred to as penetration, or there is a finite probability that the photon will interact with an atom or an atom's electrons and be removed from its original path, referred to as attenuation, denoted by the term μ. The type of interactions that occur and their probabilities are tied to the energy of the photons and the density of the physical medium. The three main types of interactions x-ray photons have with matter are Raleigh scattering, Compton scattering, and photoelectric absorption. These three interactions can be seen in Figure 6.

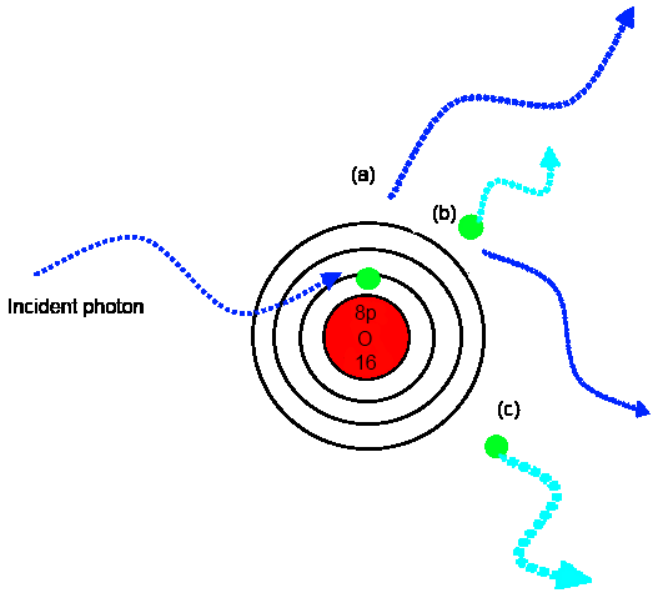

Figure 6 : X-ray interaction showing (a) Raleigh Scattering, (b) Compton Scattering, and (c) Photoelectric Effect

In Raleigh scattering the photon is absorbed by the atom in vibrational form and then almost immediately ejected again in the form of a photon of similar energy and direction as the incident photon. This type of scattering contributes to decreased contrasts in images because the photon experiences roughly no change in energy but can experience a change in direction. Raleigh scattering is more prominent in low energy x-rays in the area of 10kVp to 50kVp, such as fluoroscopy and mammography, but negligible at higher x-ray energies 50kVp and up [8]. Raleigh scattering attenuation is denoted with the term μ_R.

In Compton scattering the photon collides with an electron to ionize an electron and changes direction based on the amount of energy transferred to the ejected electron. The total momentum of the incident photon is conserved when the ejected electron is accounted for but the scattered photon will have an energy and direction different than the initial photon. Compton scattering increases with increased x-ray energy and accounts for almost all the attenuation in high energy x-rays [8]. This scattering is denoted μ_C and contributes to a lowering of image contrast if the scattered photon cannot be filtered or distinguished from unscattered or penetration x-ray photons.

Finally, in photoelectric absorption a photon ejects an electron from an atom by completely transferring its incident momentum to the electron. The electron is then emitted into the surrounding

medium where it is absorbed or can transfer its momentum to the surrounding material through collisions or Coloumbic interactions. Due to the small atomic numbers involved in organic tissue, as shown in Table 1, the probability of producing further x-ray photons is almost zero which means that photoelectric absorption produces no scattering artifacts other than high speed electrons and lower energy photons. However, photoelectric absorption probability decreases with increasing x-ray energy and the amount of energy transmitted to the x-ray target, referred to as dose, is the largest for a photoelectric interaction. The probability of this interaction is closely tied to the density of the material as well, so this mechanism is the dominant source of contrast in most images that involve bone or contrast agents in the body. Photoelectric absorption is denoted with the subscript μ_P.

The total attenuation of a material is the linear sum of all the attenuation mechanisms described above, yielding

$$\mu = \mu_R + \mu_C + \mu_P \tag{1.3}$$

X-ray images are formed when the material and energy dependant factors of for different parts of the body are exposed to an x-ray source allowing the penetrating radiation to be captured correlated to the attenuation coefficients present in the body by the formula:

$$N = N_0 \, e^{-\mu x} \tag{1.4}$$

Where N is the incident number of x-ray photons and x is the distance travelled through the image target. Note that the transmission of x-rays through matter is inherently an exponential process with respect to the distance, usually a fixed value in medical imaging, but a linear relationship to the incident photons. A good x-ray detector should capable of maintaining this linear relationship even at low photon incidence levels, called fluence levels when referring to EM radiation, in order to allow for the patient to be exposed to as low amount of x-ray photons as possible. This way the potentially damaging energy absorbed through Compton scattering and the photoelectric effect can be kept to a minimum in x-ray applications that involve longer exposures times.

Once an object has been exposed to x-ray radiation it is the job of the x-ray imager to detect the incident radiation amounts and record the detected flux over a given area and store it to be analyzed. The area of x-ray detection and capture will be the focus of this thesis.

1.4 X-ray Modalities and Imaging Areas

X-rays are high energy photons that scatter when they interact with matter and therefore cannot be focused in a manner similar to low energy photons, such as visible light. For this very reason x-ray images are usually the exact same size as the imager that takes them. Therefore one thing common to all x-ray modalities is that they must be large enough to cover the region of interest but not too large as to be prohibitively expensive.

X-ray imaging exploits the penetration and attenuation property of high energy photons through the human body and can be used in a wide variety of applications that require non-invasive or density sensitive information to be captured about the patient. The photon energy dependant factors of the attenuation coefficients and how they relate to different parts of the human body are what determine if certain energy ranges are more suitable to specific types of imaging more than others. These imaging areas, or modalities, can be separated in modern x-ray radiography to fit into roughly four categories; chest and general radiography, mammography, fluoroscopy, and x-ray computed tomography. Each type comes with its own set of design parameters and constraints that aim to optimize the function of the modality and safety of the administered dose of x-rays. Important criteria for imaging systems are detector size, pixel size, readout time, x-ray spectrum sensitivity, and dynamic range. They will be discussed and criteria for each imager will be derived in the following sections.

1.4.1 Chest and General Radiography

Chest and general radiography represent the oldest and most ubiquitous mode of x-ray imaging. This area encompasses the images used for bone analysis, tuberculosis screens, or any other general image where an x-ray image is required. A diagram of a typical chest radiograph is shown in Figure 7 to illustrate the straightforward approach of this type of x-ray image.

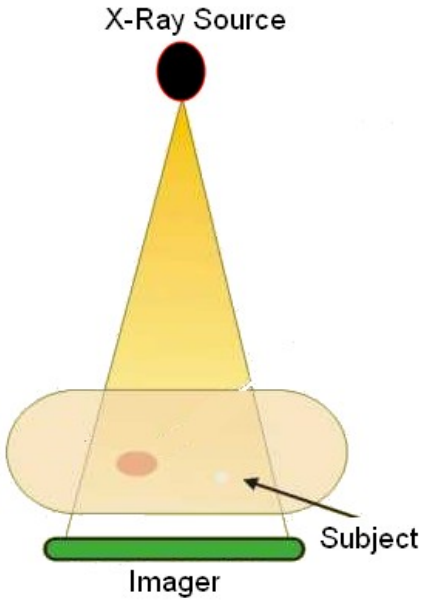

Figure 7 : General Radiography

Chest radio graphs require detectors that are significantly larger than other image types because of the large area of the average human chest. Typically, this size is around 40cm for the diagonal. Due to the size of the imager and the types of objects that will be imaged, such as bones or body lesions, an acceptable resolution of 200um is often required [11] in addition to an x-ray energy that offers acceptable contrast for bones and dense tissue, usually between 80 kVp and 120kVp on a tungsten target tube.

All stationary radiographs exhibit increased noise performance due to the presence of collimators between the subject and imager that reduce the probability of detecting a scattered photon due to Compton or Raleigh scattering that causes the x-ray to change direction. In static radiography the detected scattered to primary penetrating photon ratio is about 0.05 to 0.15. Further improvements to reduce this number would involve incorporating the ability to distinguish photon energies from each other [12].

Traditionally these types of radiographs were taken one at a time with a radiologist repositioning the patient between each image and setting up the x-ray generator as needed. This translates into an image time requirement that is not really defined. However, if the radiologist would like an opportunity to quickly grade the quality of the captured image than something on the order of a few seconds is required.

1.4.2 Mammography

Mammography involves the specific imaging of breast tissue. Due to the size and composition of the human breast this imposes different requirements than general radiography. A diagram depicting a typical mammographic setup can be seen in Figure 8.

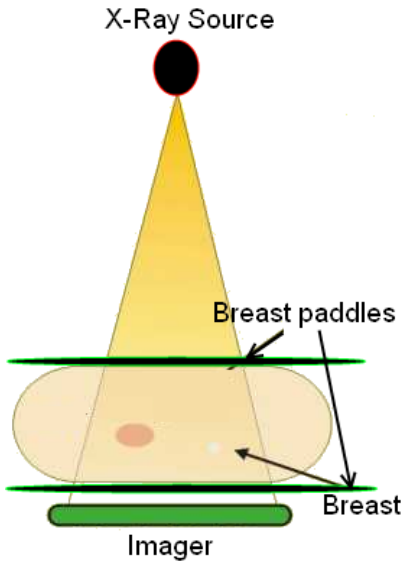

Figure 8 : Mammography

In mammography the lesions and calcifications being sought require that the minimum resolution to be much smaller than general radiography, usually on the order of 50um, but over a smaller area, usually around 25cm in diagonal [13]. In addition to a different minimum resolution, the energy used in mammography is lower because this generates higher contrast through larger absorption in the breast, roughly 40kVp on a molybdenum target tube.

Due to the pressure and alignment of the breast while this image is being taken the image time has no hard limitation imposed by the speed of the imager itself, but something on the order of a few seconds is preferred as well.

1.4.3 Fluoroscopy

Fluoroscopy is real time x-ray imaging that is used for surgery or internal observations that aid in delicate operations or diagnosing a condition with a patient that simply cannot be described in a static image. Due

to the requirement of real time display fluoroscopy represents one of the fastest and difficult areas to design for. In fluoroscopy, the patient usually lies on a table in between the x-ray source and the imaging device as shown in Figure 9. The x-ray source, table, imager, and screen are usually comprised of a single dedicated housing that the patient is inserted into for the duration of the operation.

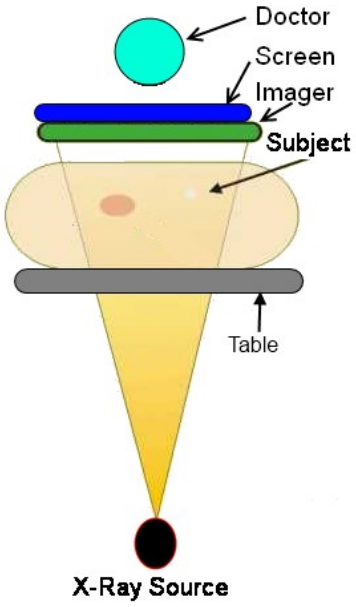

Figure 9 : Fluoroscopy

Important metrics for this type of imaging are the sensitivity, readout speed, image distortion, and low flux noise performance of the imaging device. The limitations in fluoroscopy come from the x-ray energy absorbed by a body when exposed. Fluoroscopy typically uses a 70kVp exposure with more than 300 times less x-ray flux than chest radiography [13]. The reason that the rate is lower is because the doctor and patient will be exposed to the x-ray beam for a prolonged duration which can be up to tens of minutes. While being exposed to x-rays, the imager needs to be capable of displaying a corresponding x-ray intensity picture in real time to the doctor. In order for this image to appear natural and relevant to the doctor a frame rate of roughly 30 Hz is necessary with any increase over that rate an added benefit that enables quicker and more precise operations to take place [13].

Ideally, fluoroscopic imagers are operated in a region where the device now becomes quantum noise limited. A quantum noise limitation is imposed by quantum mechanics and deals with the probabilities of photon emission, interaction, and detection on an individual basis which results in random

variations in photon flux that cannot be avoided. Dealing with the low flux of x-rays is often overcome by using larger pixel sizes that allow for more photos to be collected in the same area or a higher concentration of photons which reduces the fluctuation amount due to this effect. In digital imaging, however, there are ways to correct for quantum noise limitations in some situations by methods such as frame averaging and smoothing. This reduces the need for such large pixels and allows for smaller pixels to be used that will improve the resolution of the detector without being overcome by noise at the low x-ray levels used [13].

1.4.4 X-Ray Computed Tomography

The ability to perform mathematical analysis on x-ray image data has was actually invented and completed in theory even before the first digital imager was made but it was only the computer and digital flat panel detector that made 3-D reconstruction possible for medical applications [12]. In X-ray computed tomography (CT) the x-ray source and detector are rotated around an object while continuously capturing image data as shown in Figure 10.

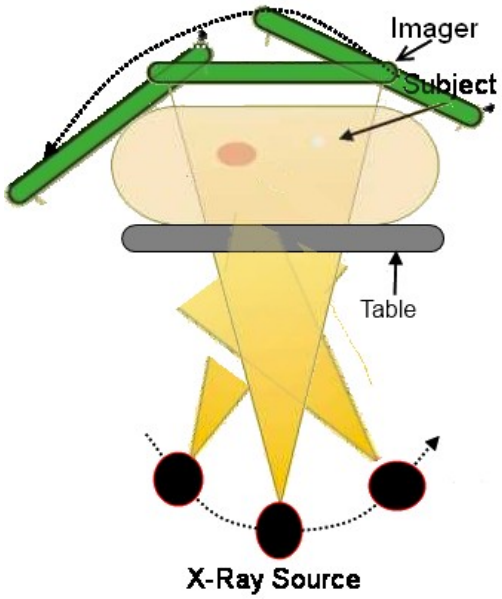

Figure 10 : Computed Tomography

Once the data is recorded a mathematical technique, called the Radon transform, can be used that allows depth and attenuation data to be computed and reconstructed onto a 3-D model that represents a depth and

density mapping of the object being imaged. Modern CT scanners are capable of rotating in a helical fashion while high speed imagers record the X-ray data. This allows for the image to be taken faster which has the effect of increasing image resolution due to smaller patient movements during the imaging process and lowering the patient dose, as the time required capturing the image, and therefore the time the subject is exposed to radiation, is reduced as well. The lower time required for each scan also saves money due to the x-ray tube having to be operated for less time.

The drawback to the speed, however, is that the noise in each pixel is increased due to the lack of collimation. In static radiography collimators can be used to filter out Compton and Raleigh scattered photons. CT cone beam scanners can not use collimation which raises the scatter to primary ratio to roughly 0.4-2 [12]. This fact usually leads CT scanners to use higher x-ray energies, in the range of 70kVp to 140 kVp, which have lower attenuation for human tissue but are more damaging due to the sheer amount of images that are needed to be taken in a scan. The ability to filter and distinguish between scattered and primary photons would enable a CT scanner to increase resolution and decrease noise with no additional modifications.

As an additional piece on CT scanners, the concept of 3-D reconstruction based on images from multiple angles has spread to conventional radiography as well in a mode called tomosynthesis. In tomosynthesis a sequence of images is taken, usually two or three, with a slight spatial and angular separation between each image. The images are then combined offline to help create an additional depth based contrast that gives certain body parts more definition making observations, and diagnosis, easier for a radiologist to make [14]. Tomosynthesis is more focused on traditional radiography and mammography, however, than where CT scanners are typically used and so the requirements for this modality will be imposed on the imaging devices for those modes. For an imaging device to adapt to this new modality a fast framerate is required in order to minimize patient movements which can destroy any gains in image quality.

1.5 High speed X-ray imagers

From the criteria related to each of the imaging modalities above design criteria can be summarized in Table 2 shown below. In addition to the descriptive limitations discussed previously additional requirements are now listed that detail the mean exposure and noise levels that are considered tolerable for each modality and how they translate into circuits.

Table 2 : Specifications for Digital X-Ray Imaging Systems [13]

	General	Mammography	Fluoroscopy	CT
Detector Size	35cmx43cm	18cmx24cm	25cmx25cm	20cmx20cm
Pixel Size (square)	200um	50um	250um	80um
Readout Speed	2 Hz	2 Hz	30 Hz	10 Hz
X-ray Spectrum	120 kVp	40 kVp	70 kVp	80-140 kVp
Mean Exposure	300uR	12mR	1uR	500mR
Photon Fluence (photons/mm^2/mR)	$2.3x10^5$	$4.77x10^4$	$1.98x10^5$	$2.5x10^5$
Noise Level	6uR	60uR	0.1uR	100uR

Using the values in the table as design parameters an imaging device can be designed and optimized for each modality. With the introduction of digital tomosythesis techniques the need to create high speed imagers that can be used for standard radiography images in addition to being fast and flexible enough to capture the necessary images in a short period of time represents a new market. The imagers that fill these requirements should also be able to be more sensitive and efficient with the x-ray radiation the patient is exposed to so that the administered dose can be lowered without compromising image quality.

Not mentioned in this introduction is an area of x-ray imaging that directly benefits from the advances in medical x-ray imaging, namely security, industrial, and scientific x-ray imaging that includes fields such as space imaging, x-ray crystallography, automatic defect analysis, patent infringement law, and national security [6]. These areas represent a discussion that would warrant an entire chapter for themselves, would create different criteria with a different focus than those discussed in Table 1, and so while of interest to the author will not be covered in this thesis.

1.6 Summary and Thesis Organization

This chapter presented a history of x-rays and a physical understanding of how they are created, captured, and used to create images. Different medical x-ray techniques were detailed that represent different areas in radiography. The different radiographic modalities result in different specifications that determine what

constitutes a satisfactory or excellent imaging device with respect to its minimum pixel size, noise resolution, and x-ray spectrum response. Finally, the new market segment created by tomosynthesis represents a new area of x-ray imaging devices that can filled by a new type of imaging device that offers high speed, low noise, and high resolution.

This thesis will be to investigate and optimize a novel x-ray circuit for low noise and fast operation for radiography or real time imaging modalities.

Chapter 2 will discuss the components that comprise an x-ray imaging system and explain the design decisions made early on in the design process. These factors include the conversion mechanism, pixel architecture, and circuit materials.

Chapter 3 will discuss the design and simulation of the circuit including parameters that were optimized or altered. It will also include issues associated with the electronics and material interfacing between the circuit and extra processing required.

Chapter 4 presents test data of the chip including tests designed and carried out solely for the course of this thesis.

Chapter 5 will discuss lessons and experience learned that should go into designing an imager for future use. The issues and workarounds will be discussed and contrasted with mechanisms designed to avoid them and suggestions will be given, along with how they would be implemented, that will allow for this research to be more commercially viable.

With these factors in place the next chapter will cover how x-rays are converted into a measurable signal to meet the criteria established in this chapter when forming a medical image.

Chapter 2
Detector Structures, Amorphous Photoconductors and Backplanes for Large Area Imaging

This section will give an overview into the components that make a digital x-ray imaging device and provide rational into why one choice was taken when developing the imager over another. A system overview will break down the system into three main components that are present in every imager; x-ray conversion, signal detection, and readout section will be described and compared. All focus will be placed on digital mechanisms for achieving these actions as a digital system is the only feasible approach to the computerized modalities described in 1.4.

Different modes of x-ray conversion will be discussed that will give insight into optimizations that can be implemented in this first stage. The two types of x-ray conversion will be compared in addition to a discussion on amorphous selenium which represents a new material in this field that is the material of focus for this thesis.

Next, a discussion on two types of semiconductors will highlight differences and similarities between amorphous and crystalline semiconductors. This information will be used to decide between proper applications of one over the other.

Finally, detector structures and back planes responsible for signal detection will be detailed and compared. Vertical and horizontal layouts are discussed along with the applications and merits for each. CMOS and amorphous backplanes are compared for speed, noise performance, compatibility, and cost.

2.1 Large Area Imaging Systems

An imaging system is a system that contains the necessary components to detect incident radiation, convert the radiation to an intermediate exchange mechanism, and then transmit the information to an external source. Digital imaging systems contain multiple components that must cooperate and work together in order to produce an image. The basic diagram of an imaging system can be seen in Figure 11.

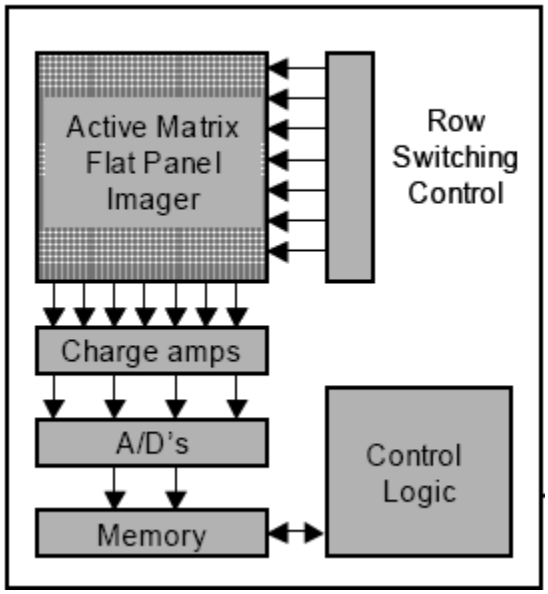

Figure 11 : Basic digital imaging system [15]

Whether large or small area all digital imaging systems have the same basic block diagram as shown. The active matrix flat panel portion of the imaging system will be the focus of this thesis as the logic circuits, amplifiers, and timing required to operate the imager itself have constituted many other works. Selecting appropriate components and optimizing the timings of the peripheral circuits will be assumed and instead the focus of design will be given to the active matrix flat panel portion of this system. A further breakdown of this component can be summarized in Figure 12, which details the components common to all digital active matrix flat panels, whether large area or single pixel [16].

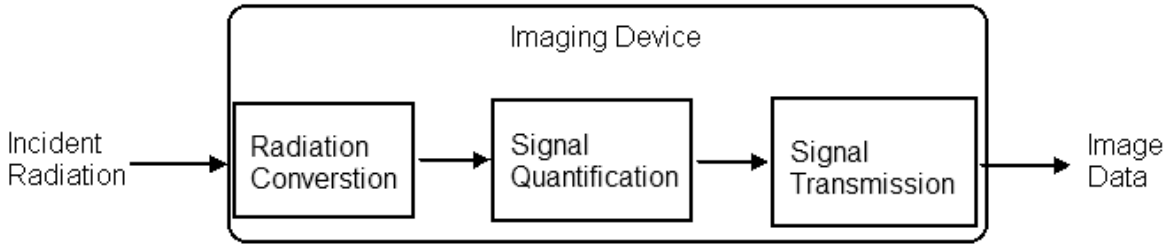

Figure 12 : Imager System Components

Large area imagers systems are unique in the problems they face are problematic to deal with in each step of the system. Due to the sizes of the imagers required as described in Table 2, converting incident radiation uniformly over the entire panel is crucial to producing a meaningful x-ray image. Due to the need to keep radiation doses low and exposure time short, efficient and reliable conversion of the data collected is equally as important. In addition to these issues the need to be able to transmit the data quickly becomes an additional constraint when the speed requirements of real time x-ray imaging or tomosynthesis are factored in. For these reasons an understanding and analysis of the three system areas is necessary to design an x-ray imager, starting with the radiation conversion.

2.2 Indirect and direct detection

Radiation conversion mechanisms for digital imaging can be roughly separated into two categories that describe how x-rays are transduced into a detectible signal. The first category is called indirect conversion. This mode uses a phosphor that, when exposed to x-ray radiation, produces photons of a different wavelength using the same mechanisms described in section 1.3. The second category is called direct conversion due to the generation of electron-hole pairs when exposed to x-ray radiation. Direct and indirect conversion mechanisms are both shown Figure 13.

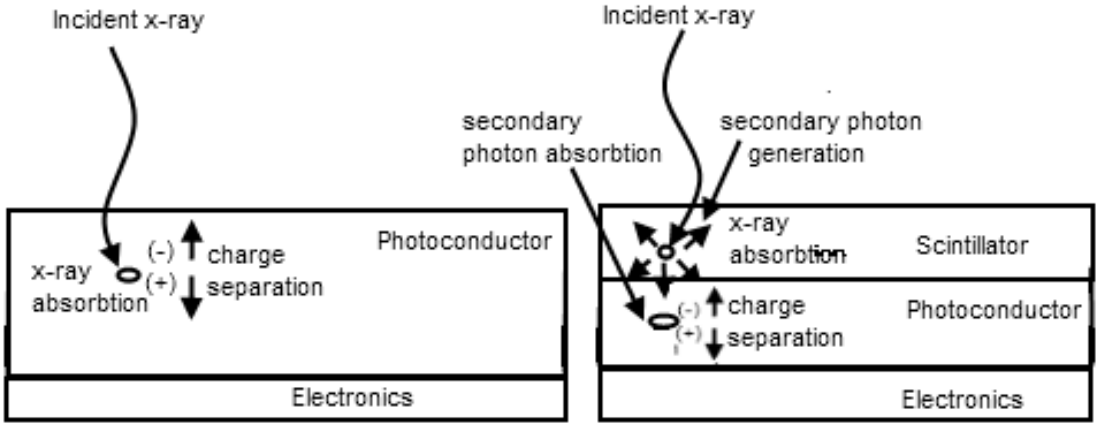

Figure 13 : Direct conversion (left) vs indirect conversion (right)

The choice of conversion mechanism depends on the desired response and speed characteristics that the imager requires. Currently, for the high speed operation required in tomosythesis and fluoroscopy the use of indirect conversion detectors is common due to the speed and leakage challenges associated with direct conversion materials and interfacing them to the electronics [17] [18]. For this reason a focus will be

placed on indirect conversion mechanisms and parameters will be optimized to design a detector using indirect detection.

2.2.1 Indirect Conversion

Indirect conversion, as shown in Figure 13, involves the use of a scintillating phosphor as the initial x-ray radiation conversation mechanism into visible light before another layer, usually a photoconductor, is used to convert the light into a measurable signal. There are two main issues encountered when using this approach. The first is that photoluminescence, or the emission of photons due to the relaxation of electrons caused by the absorption of the incident x-ray, is an inherently randomly oriented process with respect to the direction of the emitted photon that causes the light to scatter. The second problem is that the decay time of a scintillator, or the amount of time it takes for the photoluminescence to stop, can be on the order of seconds when high energy x-rays are used. Both of these problems cause motion artifacts, blurring, and reduced image quality when high speed images need to be captured [19].

Selecting a scintillator therefore involves making sure that these effects are reduced. To accomplish this, the first stage in the imaging device will involve coupling a suitable scintillator to a photodetector. X-ray scintillators have been refined over time, but a current state of the art single crystal type is made of thallium doped cesium iodide (CsI:TI). This material has a rod type structure that, when properly grown, can extend hundreds of microns long as shown in Figure 14 with the rod only being a few microns in diameter.

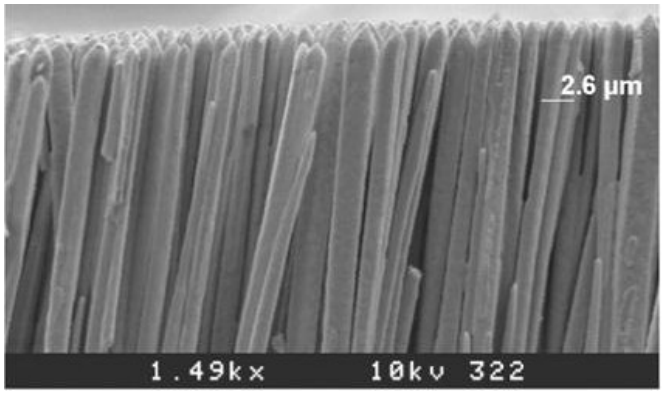

Figure 14 : SEM of CsI rods [20]

This growth serves two purposes; it allows for the scintillator to be of sufficient thickness for mammographic x-rays so that the x-rays are totally absorbed, a term called the absorbtion depth that's

related to the attenuation coefficient for a material that was discussed in 1.3 [21], and the cone rod like structure serves as a fiberoptic taper that channels most of the generated photons either up to the top of the scintillator where they can be reflected or down to the underlying photoconductor where they can be detected. This mechanism acts to reduce the blurring caused by the omni-directional photon generation at the point where the x-ray is absorbed [19]. For the energies used in mammography it is recommended that the scintillator be at least 150um thick.

In addition to utilizing crystal growth to reduce blurring and increase absorption efficiency the CsI:TI can also be optimized to improve the speed by codoping with samarium (Sm) [20] or europium (Eu) [22]. Doping with these elements has been shown to reduce the afterglow present in CsI:TI when made to absorb high energy radiation such as x-rays to less than half a millisecond without changing the photon emission spectra and quantities by significant amounts from an undoped crystal [20]. This meets the speed criteria discussed earlier and will allow for CsI:TI to be the scintillator material used in a high speed imager. The selection of a scintillating film for the imager converts x-rays into lower energy photons and still requires a mechanism to convert photons into a quantifiable signal. The output of a doped CsI:TI crystal is well documented for use in mammographic applications [19] and a graph showing the output spectrum of a scintillator of this type is shown in Figure 15.

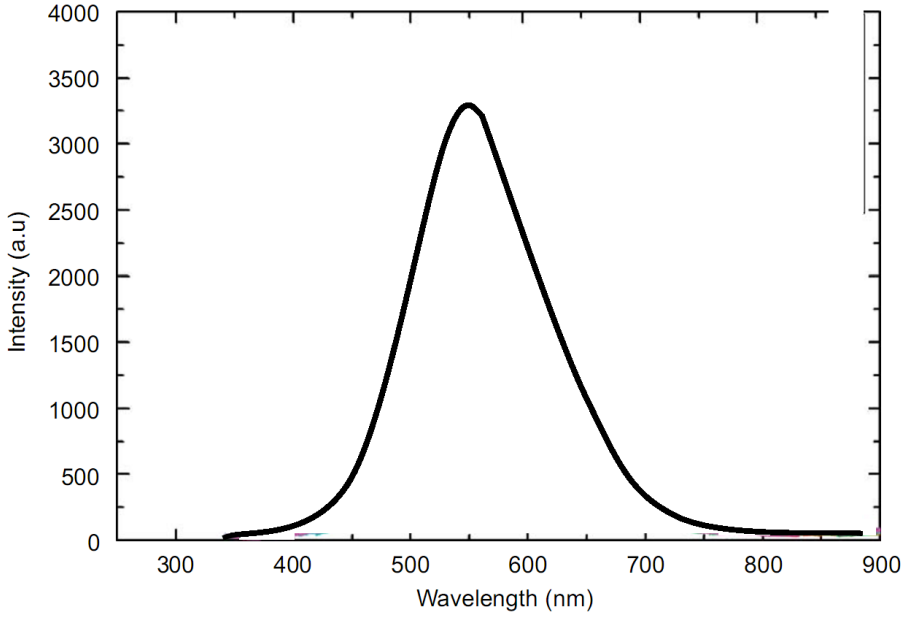

Figure 15 : Output spectrum of doped CsI:Ti scintillator [19]

Because it is not the focus of the STAR research group and therefore beyond the scope of this thesis, the choice of a Cs:TI scintillator film will be assumed to be sufficient for the first stage of radiation conversion and for purpose of this thesis while the second part of the radiation converter, the amorphous photoconductor, will be covered in 2.2.2 in much more detail.

2.2.2 Amorphous materials as Photoconductors

One of the difficulties in large area imaging is the uniformity of response that is required across the entire flat panel. In order to generate effective large area imagers amorphous semiconductors are commonly employed as photoconductors and have been widely used since Xerox pioneered the technology in the early 1980's for use in photocopiers. Since then, amorphous semiconductors have been used in applications such as cameras, televisions, scanners, and even direct x-ray detectors [23]. Amorphous materials have advantages related to cost and ease of integration with other materials and substrates because the processing temperatures, contamination conditions, and facilities required for the deposition and use of these materials is much lower than polycrystalline or crystalline materials.

The choice of utilizing a CsI:TI scintillating film for a high speed x-ray imager means that the choice of photoconductor must be optimized and understood as well so that the efficiency of the two can be maximized. This is due to the linear property of imaging systems, which can also be applied to x-ray imagers, which allows you to model each stage in your design as a linear transfer function with the resultant signal being the product of each the individual stages [24]. Matching and maximizing each step in the chain of imaging components will therefore give the best result.

Utilizing this modeling property we can then develop a strategy that integrates an understanding of amorphous semiconductors with the scintillating film that will result in a higher quality imaging device. Also, because the discussion of amorphous semiconductors will be of focus when designing the backplane, or circuitry, of the imager it is important that amorphous materials be given an overview.

2.2.3 Material Arrangement and Properties of Amorphous Semiconductors

The most thorough and relevant framework for understanding amorphous materials can be approached by applying a quantum mechanical analysis to the arrangement of atoms and orbital electrons as understood earlier in section 1.2. The result of this theory, initially applied to crystalline conducting, insulating, or semiconducting materials results in a band theory that is capable of predicting electron distributions and

functional aspects of the material such as band gaps and carrier mobility. The band theory relies on the well ordered structure and electron orbitals of the crystalline material to separate any material into three distinct bands that can be quantified by a function called the density of states, g(E), which defines the number of electron states that can be occupied per unit energy. This function separates the available energy states of a solid into three bands called the conduction band, where electrons are free to move along in the crystal at a speed determined by crystal lattice and electron affinity properties, the valence band, where electrons are covalently bound to the atoms in the crystal, and the band gap, the space in between the two bands that specifies the energy an electron has to obtain or lose before changing bands. A diagram of well ordered crystal and the band theory representations of a conductor, insulator, and semiconductor are shown in Figure 16.

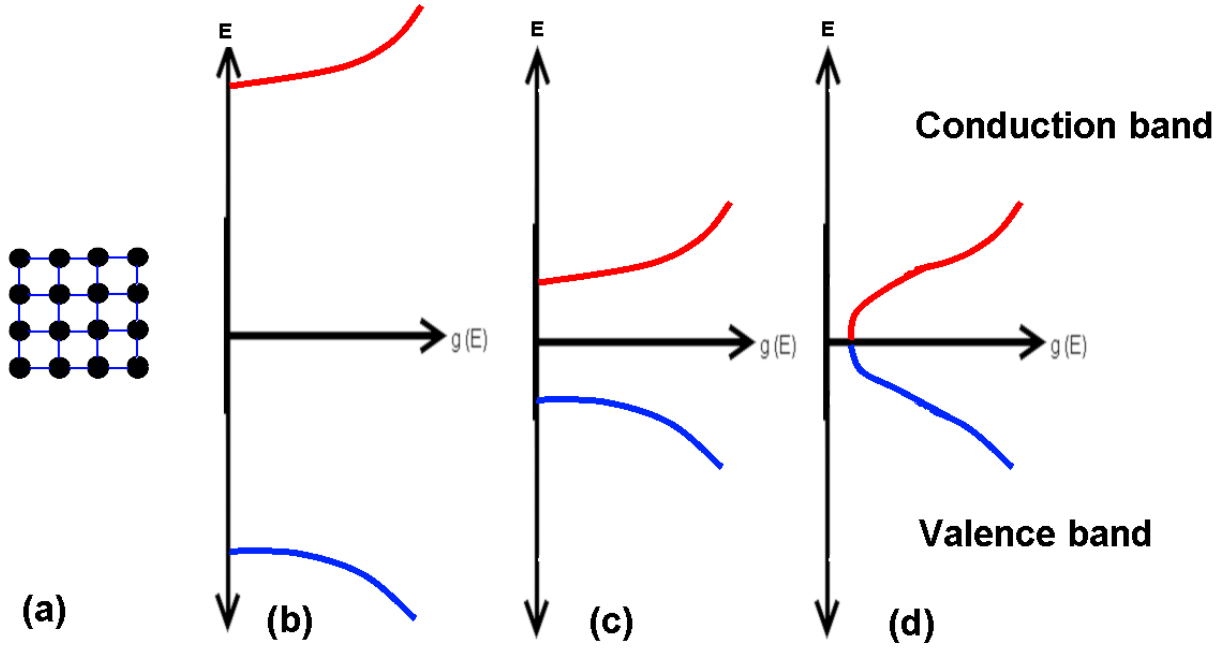

Figure 16 : Diagram of (a) crystalline solid and resultant density of states for (b) insulators, (c) semiconductors, and (d) conductors. The zero crossing on the Y axis denotes the Fermi level.

This figure can also be used to roughly explain how semi-conduction occurs in the crystalline case. At a given temperature, T, for a semiconducting material it can be said that the material exists at the ground state, a state in which all the valence band is occupied and the conduction band is empty. This ground state is usually demarcated with a line called the Fermi energy level that represents roughly, at T = 0*K, a midpoint between each band. When a free electron is generated, that is to say some event causes an

electron from the valence bond to be sufficiently energized and motivated to cross the band gap present in the semiconductor, a hole is also created in the valence bond where the electron used to be creating two charged carriers, one in each band.

In this charged condition an electric field can be applied across the semiconductor that draws the conduction band electron toward the cathode, the positively biased terminal, and moves the hole toward the anode, the negatively biased terminal. This is the idealized model in which crystalline semiconductors operate. Conductors, in which no band gap exists so carriers are free to move in either direction without having to be generated, and insulating materials, where the band gap is so large that practically no carriers are ever generated, are extensions of this band model to either extreme where the bands touch or grow further apart.

It has been shown that amorphous materials possess many of the same properties and characteristics of their crystalline counterparts when analyzed for short range order [25] and a model to extend this useful density of states equation has been developed that allows for many of the crystalline design and simulation techniques to be carried over into amorphous material analysis and characterization [26]. In this model the assumption is that short range order is present in the solid and that disturbances in the bonding network can be classified as overcoordinated or undercordinated.

Overcoordinated bonds represent bonds that have a more tightly spaced bonding arrangement than it would have in a normal crystalline structure whereas undercoordinated bonds have a looser bonding arrangement than they would in a crystalline solid. Starting from this, and then factoring in other defect states such as dangling bonds and material impurities, the extended the DOS model that is created contains localized tails, that is to say extensions of the conduction and valence bands that are randomly present only over small areas in the amorphous solid, in which one band appears to have crossed into the other but the material does not behave as a conductor due to the fact that these bonds are highly localized and do not provide the energy free barrier present in conductors. Figure 17 shows this modified DOS graphically when taking into account the different bond coordinations, dangling bonds, and impurities in amorphous solids.

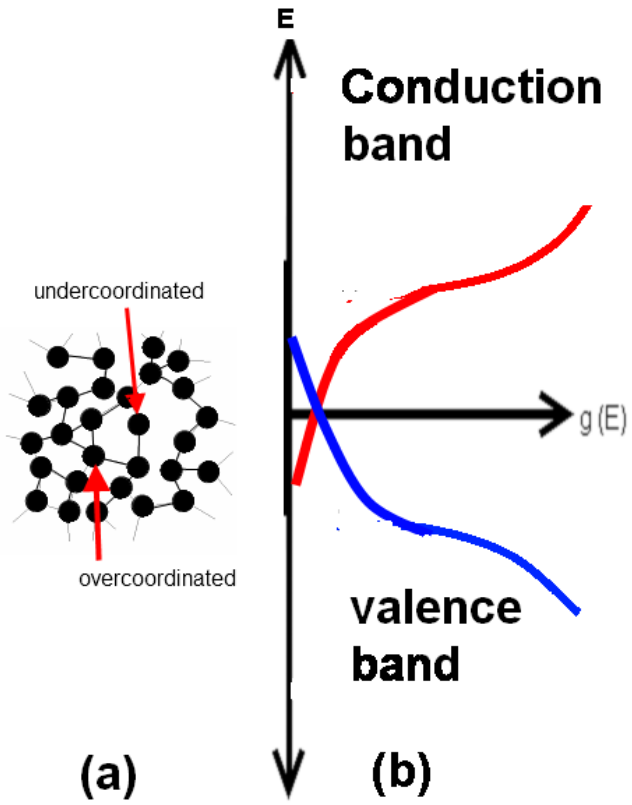

Figure 17 : Diagram of (a) amorphous coordination and (b) amorphous density of states. The zero crossing on the Y axis denotes the Fermi level.

This figure shows that when an amorphous semiconductor possesses a carrier, either an electron in the conduction band or a hole in the valence band, the charged carrier can move along the lattice under an applied field. While moving, however, it faces a finite probability of moving to an atom or location in the amorphous solid where its energy would be lowered, or raised, sufficiently that the carrier would not be energetically coerced by the applied field to move further along either of the bands, in essence becoming trapped. Locations in a material where carriers can essentially become stuck, and no longer contribute to the current flow in the semiconductor, are called traps. The presence of traps is the prime material differentiator that can be used to explain many of the lower mobility and metastable properties of an amorphous semiconductor that change over time when compared to crystalline semiconductors.

In these explanations it was assumed that the semiconductor materials were not affected, or limited, by the presence of the generated charges or other carriers present at temperatures above absolute

zero. Temperature, being an actual measure for the amount of vibrational energy in a system, has the effect of generating free carriers as it increases. In all semiconductors this has the effect called thermal recombination in which the conduction band and the valence band are constantly filled with carriers that exist for a time period, called the carrier lifetime τ, before becoming annihilated by re-crossing the band gap to join with a nearby hole; a consequence of Columbic attractions between the opposite carriers and the desire of the material to return to the ground state.

There can exist conditions, whether due to large temperatures, excessive traps, or large currents, where the conduction bands and valence bands become space charge limited. In space charge limited operations the presence of too many carriers in each band begins to actually effect the mobility and shape of the bands locally. This has the effect of saturating either band causing the mobility of that band to be reduced. This can happen to the conduction band, the valence band, or both bands simultaneously but has the same consequence of lowering the amount of current the semiconductor is capable of carrying by modulating the transport properties of the band that become space charge limited [27]. In amorphous semiconductors traps directly contribute to space charge limited situations because they saturate the bands without contributing to the device current. This has the effect of lowering the gain, sensitivity, speed, and ultimately the usefulness of amorphous semiconductors in certain applications.

2.2.4 Stabilized Amorphous Selenium as a Photoconductor

Amorphous selenium (a-Se) has served as photoconductor for the photocopying industry for decades and represents a viable material for integration with a large flat panel imager. Selenium itself is a group VI element, with an atomic number of 34, which has an electron arrangement that leaves two open bonding sites on the outer orbital that occur at 105° bond angles to each other on one face of the atom [28].

In the crystalline arrangement these bond angles alternate with the next selenium atom creating a uniform chain with stable inter-atomic distances to the other atoms in the chain in a left hand, right hand bonding arrangement. However, in the amorphous case, these bond angles deviate slightly from 105° and no longer alternate in an order manner, instead they twist to distort any stable lattice and occur randomly. Also, the selenium bonding orbitals can form a covalently linked third bonding site, called an interstitial, to further distort any apparent lattice structure. This results in inter-atomic distances that are not fixed and selenium chain structures that can occur in sequenced rings, chains, or any combination of the two.

Se as a photoconductor must occur in the amorphous state because once the material crystallizes it loses the photoconductive properties associated with it. To maintain the amorphous structure, then, precautions and steps are taken during the design, deposition and handling of the material. Pure a-Se itself is unstable and crystallizes, due to ambient conditions, in periods that can range from days, months, to years. Precautions taken to insure that the selenium does not crystallize include alloying the material with known compounds to restrict or reduce crystallization, restrictions on processing temperatures, and restrictions on substrates for deposition.

To deposit an a-Se photoconductive layer the desired alloy - usually a mixture of selenium, arsenic (~0.5% by weight), and chlorine (~40 parts per million) – is placed inside a vacuum chamber that operates as a resistive evaporation chamber as shown in Figure 18. The exact composition of the a-Se is unknown as it is sourced from a proprietary supplier that wishes to keep this information a trade secret.

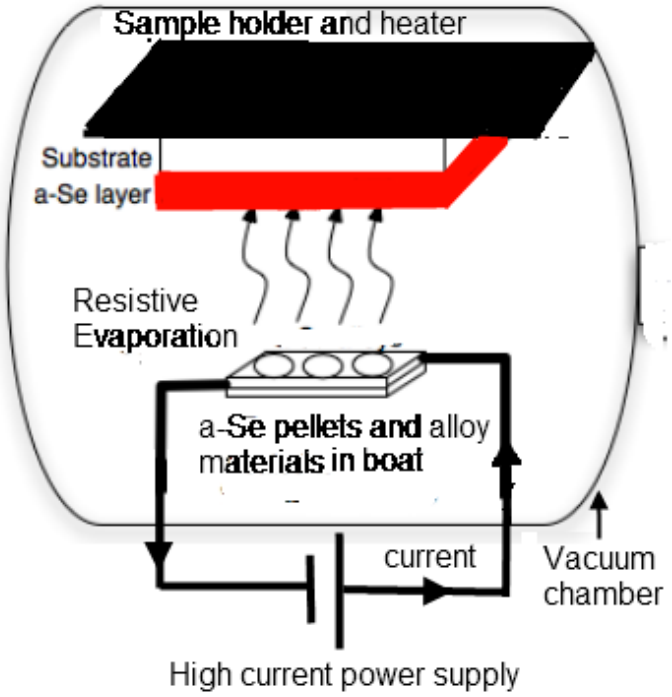

Figure 18 : a-Se Deposition

The sample holder is heated to a temperature, usually between 50°C and 65°C while the chamber is totally evacuated to near vacuum pressure. The temperature control on the substrate is essential because

the glass transition temperature, or the temperature at which selenium begins to transition into a crystalline material, is known to be roughly just above this region. Also, it is known that the temperature of the substrate affects the electrical and optical properties of a-Se during the operation of the device [29].

The selenium alloy is then heated to 250°C and melts into a gas that evaporates onto the substrate suspended overhead. This a-Se layer grows depending on the current supplied, vacuum pressure, and exposed solid angle of the substrate to the a-Se boat. Typical evaporation rates are in the area of 2um / minute.

Once the desired thickness of a-Se has been deposited the sample is usually annealed at the substrate temperature for a number of hours before being processed further. After this stage additional processing and deposition can be done to the sample if the requirements of not raising the temperature past the glassing point and not introducing stress to the selenium interface can be met. The difficult requirements attached to post processing a-Se for use in circuits is one of the problems this thesis aims to address and will be discussed in 2.3.

2.2.4.1 Electrical and Photoconductive Properties of a-Se

When operating in dark conditions and under a DC bias a-Se behaves as a highly resistive material. This property is beneficial for photo-detectors as it leads to a low dark current which is necessary for low noise and high dynamic range imagers. The conductivity of a-Se increases significantly when exposed to light due to the absorption of the light and generation of electron hole pairs, which is what makes a-Se a photoconductive material.

The band gap of a-Se is known to be roughly 2.1 eV, which corresponds to an optical wavelength of 592nm. This means that incident light below this energy is exponentially less likely to be absorbed and that incident light above this energy has a probability of being absorbed that is modeled by the absorption coefficient, α. Stabilized a-Se has an absorption coefficient that can be seen in Figure 19. The absorption coefficient is a number that states for a given wavelength what the probability incident light intensity will be absorbed to 36% of its original intensity.

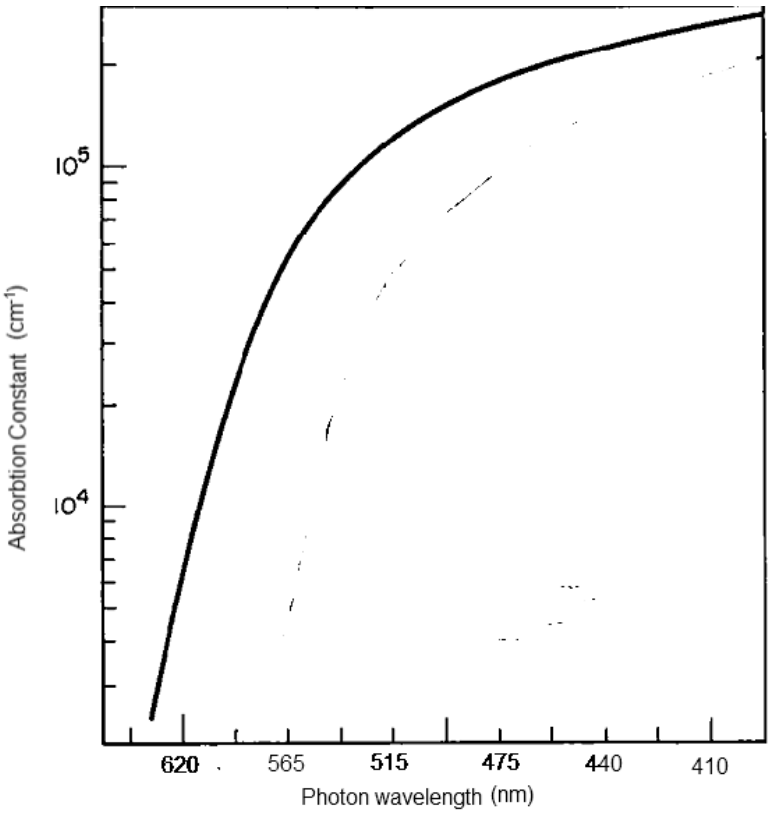

Figure 19 : a-Se absorption coefficient data [30]

This absorption coefficient can be used to determine an appropriate thickness of material so that the emitted light of the CsI:Ti scintillator will be fully absorbed. The peak emission of the scintillator in Figure 15 is roughly 550nm, so this wavelength will be used to determine the thickness. To solve for the appropriate thickness required a concept known as the absorption depth is used, which is defined as:

$$D = \frac{1}{\propto} \tag{2.1}$$

Using the values absorption coefficient values for a-Se we can calculate an appropriate absorption depth to be 1.65um. If 95% absorption is required the attenuation relationship described by equation

(1.4 so that the thickness can be increased to 2um, increasing the sensitivity of the device. The thickness of the photoconductive layer cannot be made arbitrarily thick, however, because absorption of photons and the generation of electron-hole pairs is a competing process with the phenomenon known as recombination. In recombination, if an electron hole pair cannot be collected in a certain amount of time after being generated it will either become trapped or recombine,

effectively wasting the absorbed photon. The ratio of capture and separation of the electron-hole pair is referred to as the quantum efficiency, η, of a material.

a-Se exhibits an extremely strong dependence of the quantum efficiency to the applied electric field which can be explained by the Onsager theory for disassociation of photo-generated charges [30]. In this model, the charges must be pulled apart and separated quickly so that the Coloumbic attraction can be overcome before recombination occurs. The factors that help determine appropriate thickness of a-Se are the carrier mobility, μ, and lifetime, τ. When these two factors are multiplied we get something called the effective carrier range which is an approximate measure as to how far a carrier can move in a material before recombining. Table 3 shows the hole and electron mobilities along with the associated ranges typically found in a-Se and a-Si:H, a material that will be discussed in section 2.2.5 [29][32].

Table 3 : Mobility, Lifetime, and Range of a-Se and a-Si Carriers

Property	a-Se	a-Si:H
Hole mobility (μ_h) (cm^2 / V * s)	0.13	0.3
Electron mobility (μ_e) (cm^2 / V * s)	0.008	2
Hole lifetime (τ_h) (μs)	~100	~15
Electron lifetime (τ_e) (μs)	~500	~2
Hole range ($\mu_h * \tau_h$) (cm^2 / V)	$13x10^{-6}$	$4.5x10^{-6}$
Electron range ($\mu_e * \tau_e$) (cm^2 / V)	$4x10^{-6}$	$4x10^{-6}$

From the table we can see that in order to keep the probability of recombination low in the photoconductor at a given field bias that the collection distances should be kept under a maximum amount. Also subtly disclosed in this table is that a-Se is more suited as a p-transport material in which the motion of holes is preferred to the motion of electrons.

For a-Se, which is typically biased at values above 5 V/um we see that the value for the a-Se thickness chosen as 2um is much less than the 13um as the hole range and 4um as the electron range.

2.2.5 Amorphous Silicon as a Photoconductor

Much like the development of a-Se, hydrogenated amorphous silicon (a-Si:H) has been studied and developed extensively since the 1970's as a semiconductor and photoconductor [33]. Silicon itself, atomic number 14, is one of the most abundant materials on earth and has four valence electrons which lead to four potential bonding sites for each atom. This lends itself to the ability to be doped by a variety of materials in order to alter the properties of the a-Si layer but also leads to the creation of many defect and unbound states. In order to tie these loose ends a-Si is commonly passivated with hydrogen gas to become a-Si:H.

The restrictions that were present on the handling and ambient conditions with a-Se are not problems for a-Si:H due to the fact that unlike a-Se, a-Si:H does not experience degraded performance when crystallized and also that a-Si has a glass temperature that occurs in excess of 600°C. The method of depositing a-Si:H is also different and is referred to as a plasma enhanced chemical vapour deposition process (PECVD). A diagram of this process is shown in Figure 20.

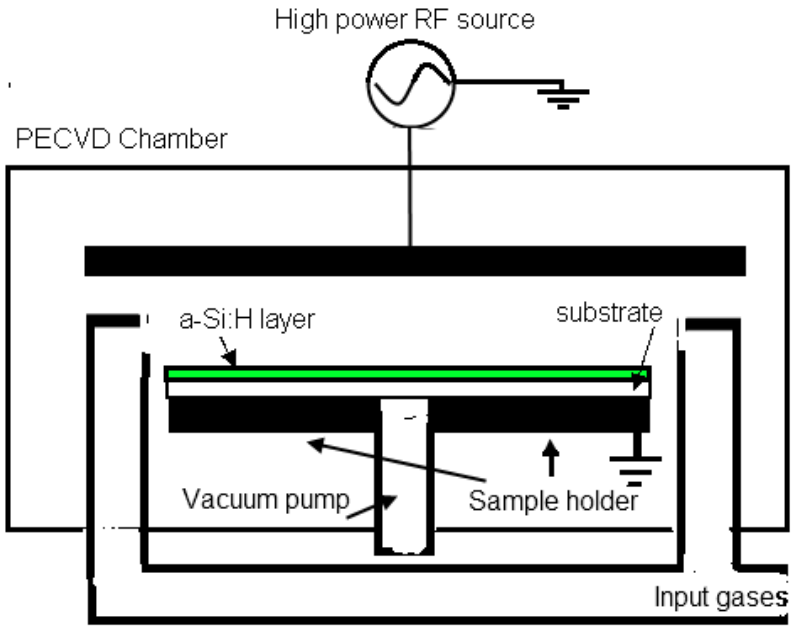

Figure 20 : PECVD chamber used for the fabrication of a-Si:H

In PECVD the substrate is heated to a temperature around 300°C and held to a ground potential while gases, usually SiH_4 and H_2 are fed into a vacuum chamber. A high powered RF source then energizes,

reducing the gas to ions, and deposits the silicon onto the target substrate. Parameters such as substrate temperature, RF power, and SiH_4 to H_2 ratios are all parameters that can be adjusted to fine tune the properties of the thin film a-Si:H that is grown onto the substrate in this process, but those are beyond the scope of this thesis.

Once the desired thickness of a-Si:H has been deposited the sample is usually annealed at an elevated temperature for a number of hours before being processed further. After this stage the sample is usually passivated which involves the deposition of an inert layer on top to protect the a-Si:H. One restriction which does exist on a-Si:H, however, is that the material is kept relatively shielded from UV light if it is to be used as a photoconductor. This is because UV light is of sufficiently high energy that it can ionize and dislodge the hydrogen atoms that are used to passivate the dangling bonds. This has the negative property of creating excessive defects in the silicon lattice structure and lowering the stable electrical performance of the a-Si:H over time. This is known as the Straebler-Wronski effect and can only be reversed by annealing the material at high temperatures [34].

2.2.5.1 Electrical and Photoconductive Properties of a-Si

The bandgap of a-Si:H is approximately 1.7eV corresponding to an absorption edge of 730nm. Contrary to crystalline silicon, a-Si:H is a direct band-gap material so that the absorption of a photon of this wavelength or higher generates a free carrier without the need for phonons, or lattice vibrations, to be present. Using the same reasoning as with the a-Se thickness calculations and the absorbtion coefficient data that can be seen in Figure 21, an optimal value for the thickness required to absorb the CsI:Ti emission is found to be 550nm for 65% or 625nm for 95% absorption.

Proceeding to check the range of carriers in a-Si:H, using the values in Table 3 the range can be found to be 4.5um and 4um for holes and electrons.

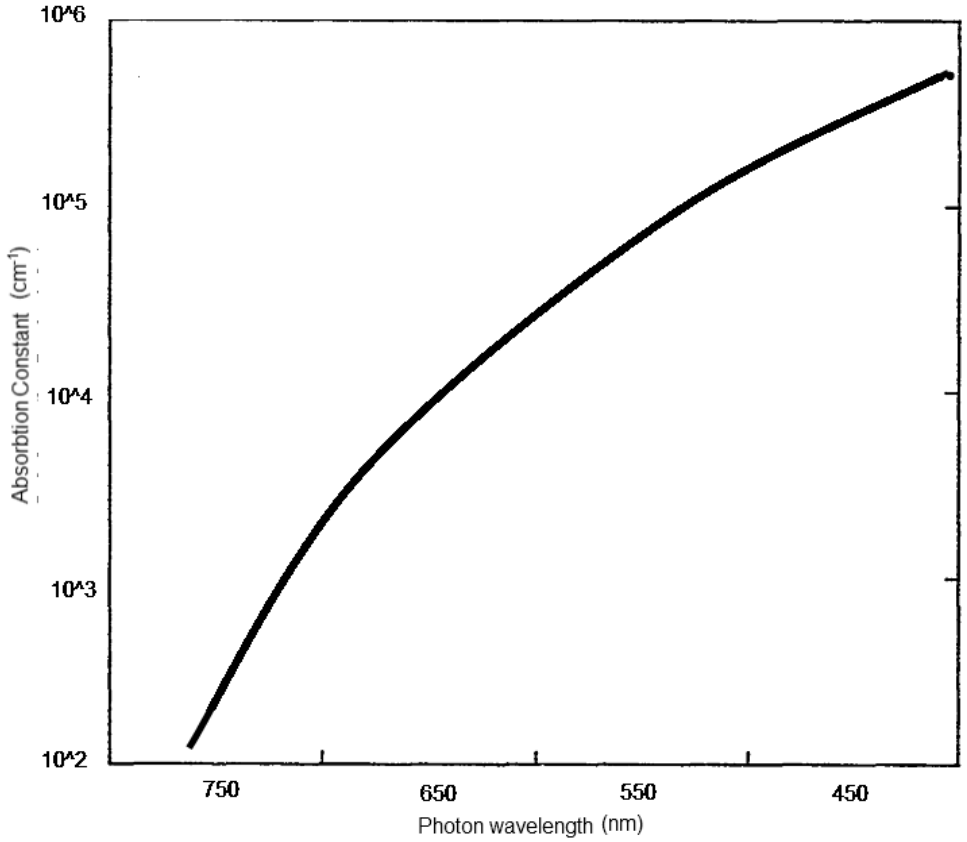

Figure 21 : a-Si absorption coefficient data [35]

2.2.6 Summary

This section has gone through how amorphous materials can be modeled, integrated, and deposited as photoconductors onto a given substrate. These photoconductors can be optimized to give large area, uniform, and effective absorption for a given optical target spectrum. Finally, the appropriate travel path length for each photoconductor before running into recombination concerns.

2.3 Detector Structure

When implementing a photodetector there are many ways that the material can be incorporated into a photoconductive detector. This section provides a quick overview into novel aspects of detector design for two types of detector alignment. Motivation and simulations are given for a vertical design in comparison to a lateral structure when amorphous photoconductors are used.

2.3.1 Vertical Detectors

The vertical detector stands as the basic method of implementing photoconductive films. This style of detector remains popular because it offers simple ways to optimize the design in addition to large area, simple fabrication techniques, maintains the ability to grow the thick detector layers for directly absorbing x-rays or targeting specific wavelengths of light, and provides virtually 100% fill factor if designed properly. In the normal vertical arrangement the photoconductor is sandwiched between two metal contacts as shown in Figure 22

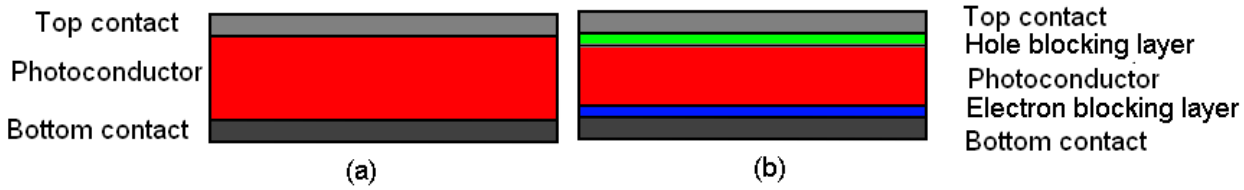

Figure 22 : Comparison of (a) basic MSM and (b) enhanced MSM vertical detectors

Incoming radiation, incident from the direction of the on the top contact, passes through the top contact and is absorbed in the photoconductor where an electron-hole pair is generated. Due to the DC biases applied between the top and bottom contacts the charged carriers separate and generate a current as they travel to the appropriate electrode.

Modifications to the basic MSM structure involve the addition of carrier blocking layers – either hole blocking layers at the anode or electron blocking layers at the cathode – that can still be deposited in a similar fashion to the film. These layers act to decrease the dark current present when biasing an amorphous semiconductor while preserving or enhancing the gain associated with placing a large electric field across the photoconductor.

The disadvantage to this structure is that it makes extensive post processing and optimization necessary in order to get a working structure. The top contact, being a metal, must be designed to be transparent or thin enough so that it does not absorb incident radiation. The metal must also be compatible with the scintillating film and must not present any electrical incompatibilities with it when biased to high voltages necessary for high gain. ITO, a soft metal usually made into the bottom contact where it can be deposited on glass first, is not a suitable metal for post processing as an evaporated or sputtered metal on top of an amorphous material which means available metals must be thin and therefore brittle to bond to.

Also, each layer in the structure represents a possible point of contamination and failure if the device is being prototyped rapidly.

2.3.2 Lateral Detectors

The lateral detector represents a compromised approach to the vertical MSM detector structure that aims to maintain the fill factor but decrease the post processing. Lateral detectors solve the shortcomings of vertical detectors at the expense of the symmetry, simplicity, and dark current that were advantages in a vertical MSM design. In a lateral detector both contacts are laid down in the same plane and the photoconductor is deposited in between and on top of them, as shown in Figure 23.

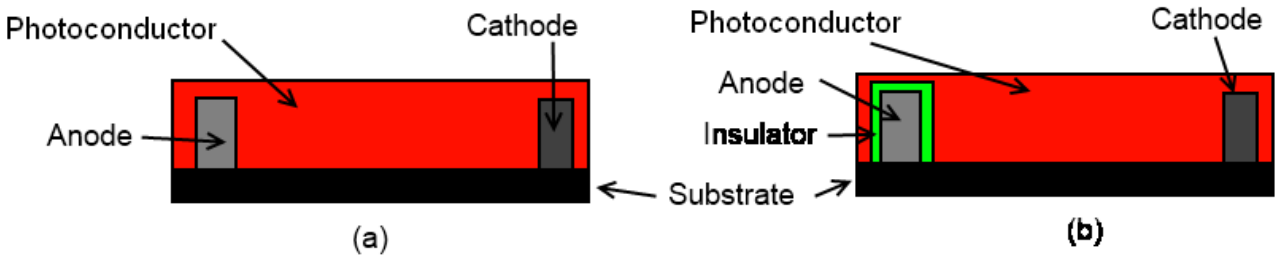

Figure 23 : Comparison of lateral detectors for (a) basic and (b) enhanced pixels

Incoming radiation approaches undisturbed from the top generates the electron hole pair in the space between the two electrodes. The charged carriers are then drawn apart and their motion is sensed as photocurrent as they traverse the gap between the electrodes.

Lateral detectors can run into aspect ratio step coverage issues when deposited to account for the acceptable carrier length discussed in Table 4. This means that to prevent the a-Se from crystallizing after being deposited onto the array the gap between the two electrodes should be sufficiently large. The space between the two electrodes cannot be made too large, however, because this requires a large bias to be applied which will increase the dark current.

If this issue can be controlled, however, lateral detectors can potentially be designed into fine comb like structures allowing for high fields to exist in the photoconductor when only small voltages are applied.

Lateral detectors suffer, however, from high dark current because there is no insulator or doped material that can reduce the DC current by insulation or diode parasitic effects. To get around this detrimental issue enhanced lateral detectors can be designed in which only one electrode is exposed to the

deposition of the photoconductor while the other contact is covered by an insulator. This, however, requires an extra processing step and introduces alignment and step coverage issues that make reliable and simple detectors difficult to fabricate.

2.3.3 Detector Structure Summary

Vertical and horizontal detector structures were contrasted with emphasis on ease of fabrication, efficiency, reliability, and ability to be integrated with the overall imager. A summary of these findings can be found in

Table 4 : Comparison of Vertical and Horizontal detector structures

	Vertical	Lateral
Detector Thickness	Adjustable	Limited by top metal
Dark Current	Low	High
Process Ease	Requires extra steps	Single step
Fill factor	100%	~100%
Circuit integration	More difficult	Simple

For the calculated thicknesses and electrical lengths of photoconductors in section 2.2.6, and based on the work of a previous group member [36] we decided to try and integrate a lateral style detector in this design. This approach represents a new and novel aspect of this thesis and should be able to provide the desired fill factor and dark current levels necessary for a good imager.

2.4 Detector Circuits and Analysis

The next stage in the design of an imager involves integrating the radiation conversion stage with the proper circuit mechanism to quantify the signal, and then transmitting the signal to where the data can be read out. This means setting up a circuit capable of reading charge from the amorphous semiconductor and also a circuit that ties the amorphous material to the readout circuit. In reference to Figure 12, this represents the last two stages of an imaging device.

This section will detail two circuit architectures commonly used in modern active matrix devices, passive pixel sensing and active pixel sensing, and properties of each one. Also, lateral and vertical methods of integrating the amorphous semiconductor with the circuit will be discussed along with the advantages and disadvantages associated with each.

2.4.1 Passive Pixel Sensing

The passive pixel sensor (PPS) remains one of the most widely used and oldest methods of reading data from a two dimensional array. Ever since it was introduced in 1967 this pixel architecture has proven robust and flexible to be used in static image devices and high frame rate applications [15]. The PPS contains a detector sensing element, a capacitive storage element, and a switchable element that can be actuated to pass a charge stored on the storage element to a data line; hence the name passive pixel sensor. A diagram of a PPS can be seen in Figure 24.

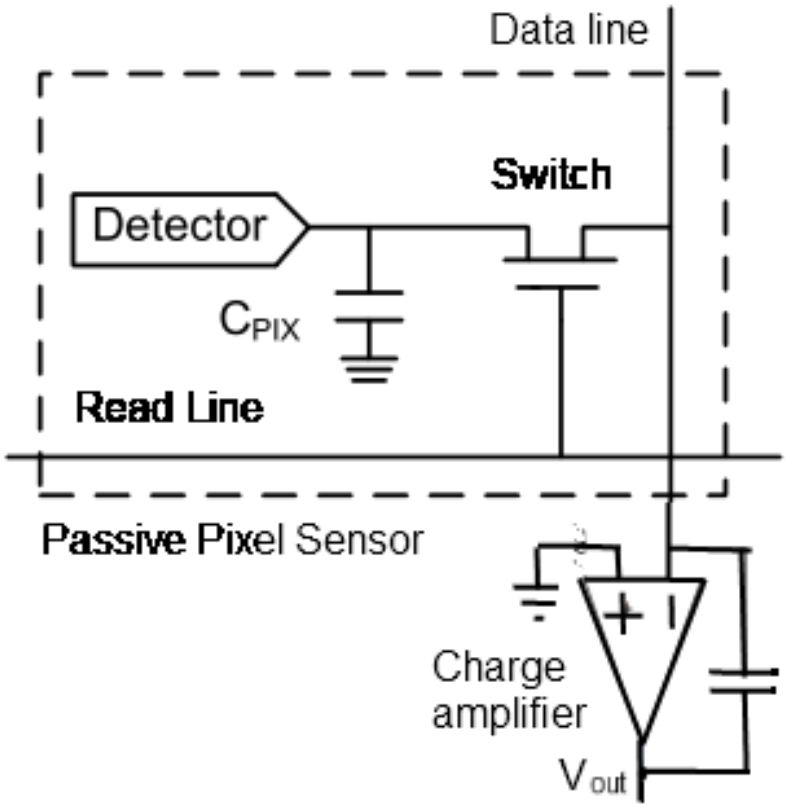

Figure 24 : Basic Passive Pixel Sensor (PPS) Circuit

The passive pixel sensor operates by switching between two modes controlled by the read line; *integrate* and *read / reset*. In integrate, the switch is turned off and the detector deposits collected charges onto C_{pix}, the pixel capacitance, proportional to the incident photon generated current in the detector, *I*. This current is the combination of two components.

$$I_t = I_{photo} + I_{dark} \tag{2.2}$$

Where I_{photo} is the current due to detected photons and I_{dark} is the quiescent current component that flows through the detector due to the voltage bias applied on the detector. Dark current in a PPS sensor has the effect of lowering the dynamic range of the detector because the relationship for a given frame time, t_{int} that determines the voltage accumulated onto C_{pix} is:

$$V = \frac{Q}{Cpix} = \frac{I_t * t_{int}}{Cpix} \tag{2.3}$$

In a PPS sensor the voltage that is accumulated has a maximum value determined by the dielectric that is used in fabricating the active matrix circuit or the breakdown voltage related to the passive switch transistor. This value can be adjusted to suit the available readout circuitry by changing C_{pix} which is equal to the sum of the material capacitance of the detector, the drain capacitance of the switch transistor, and any fringe and stray wire capacitances in the circuit. This value cannot be made arbitrarily large, however, because it can be shown that both the speed and the thermal noise level in the PPS architecture are affected with capacitances. The thermal noise generated by the pass transistor can be written as: [37]

$$N_{Transistor}{}^2 = \frac{2*K*T*C_{pix}}{q^2} \tag{2.4}$$

This component, called reset noise, when combined with the integration period time t_{int} , forms a total thermal noise voltage on the charge amplifier that can be approximated by [15]:

$$N_{th}{}^2 = C_t \frac{kT}{q^2}\left(1 - \frac{2}{\pi}\tan^{-1}\left(\frac{2*\pi*R_{on}*C_t}{t_{int}}\right)\right), \quad C_t = \frac{C_{pix}* C_{amp}}{C_{pix}+ C_{amp}} \tag{2.5}$$

Where C_t is the total data read line capacitance including the pixel capacitance and amplifier, R_{on} represents the transistor resistance that is seen between the pixel and the dataline. This noise can be reduced by reducing the total capacitances in the system or minimizing the resistance of the pass transistor.

Once data is requested and the read line is activated and the switch is turned on the pass transistor transfers the stored charge to the readout electronics. The readout rate of the PPS array is governed by the readout transistor. It can be shown that the saturated on resistance of a transistor can be approximated to be roughly (15)

$$\mathrm{R_{ON}} = \left[\frac{\mathrm{W}}{L} * u_{eff} * C_g (V_{on} - V_t) \right]^{-1} \tag{2.6}$$

Where W/L is the width to length aspect ratio of the transistor, u_{eff} is the carrier mobility of the transistor, $(V_{on} - V_t)$ is the transistor saturation voltage in operation, and C_g is the effective gate capacitance formed in the transistor channel when the gate voltage, V_{on} is applied. The finite on resistance and load capacitance of the pixel create an RC circuit that can have its time constant approximated with:

$$\tau_{ON} = R_{ON} * C_{Pix} \tag{2.7}$$

Roughly five time constants are necessary to fully transfer the accumulated charge onto the data line. Note that the readout of a PPS pixel is destructive in that the charge on the capacitor is transferred to the data line and cannot be restored. Also, note that current leakage through the transistor to the data line, parasitic capacitances that contribute to the data line load, and cross coupling due to switching in the array are all factors that can hinder the speed and low noise performance of an imager with a destructive charge based readout.

The data line itself also presents a voltage thermal noise to the PPS sensor circuit and can be modeled as [37]:

$$N_D{}^2 = \frac{k*T*R_d*C_d{}^2}{2*q^2*\tau_{ON}} \tag{2.8}$$

Showing that that the thermal noise scales quadratically for increasing data-line capacitance, which is a function of the size of the imaging device and the interconnects needed to connect the data lines to the charge amplifiers, and inversely proportional to time of integration which depends on the imaging modality. This means that PPS sensors to not scale particularly well to extremely large area arrays if the capacitances and resistances of the interconnects cannot be kept low.

The total noise of the PPS sensor would be the quadrature sum of the thermal noise in the pass transistor, N_{th}, the thermal noise of the dataline, N_D, and the noise of the charge read out amplifier, N_{amp},

$$N_t{}^2 = N_{Th}{}^2 + N_D{}^2 + N_{Amp}{}^2 \tag{2.9}$$

Ignored in this noise total are the current leakages of the detector, although it can be shown that for materials such as a-Se and a-Si:H the current noise from these sources is negligible compared to the other noise sources covered here [37].

Common values for precision charge amplifiers designed to operate on such low signals provide noise floors in the area of ~1000 electrons [15]. Note that this amplifier noise represents the noise of discrete components. The scope of this thesis will not look at optimizing this noise so that value is assumed to be fixed, although the potential to drop this noise value does exist if the amplifiers can be implemented into the imager itself, a topic that will be discussed in 2.5.2.

2.4.2 Current Mode Active Pixel Sensing

Active pixel sensing (APS) represents an approach to addressing problems associated with the PPS sensor in areas such as scaling to larger arrays, faster speeds, and lower noise performance that were discussed in 2.4.1. Two main modes of APS circuits exist, one that transmits the data to the data line as a voltage, V-APS, and one that transmits data to the data line as a current, C-APS. Only C-APS circuits will be analyzed here because V-APS circuits are not suitable to the fast sensor modalities that are involved in tomosynthesis, CT-scans, and fluoroscopy [15].

In a C-APS circuit a source following amplifier passes a current to the data line proportional to the photocurrent generated by the detector on the pixel capacitance, C_{pix}. This circuit serves two purposes. First, it decouples the collected radiation conversion data from the data line. Secondly, the source following circuit converts the detected charge into a current that can be read out by an attached charge amplifier. A diagram of the C-APS can be seen Figure 25.

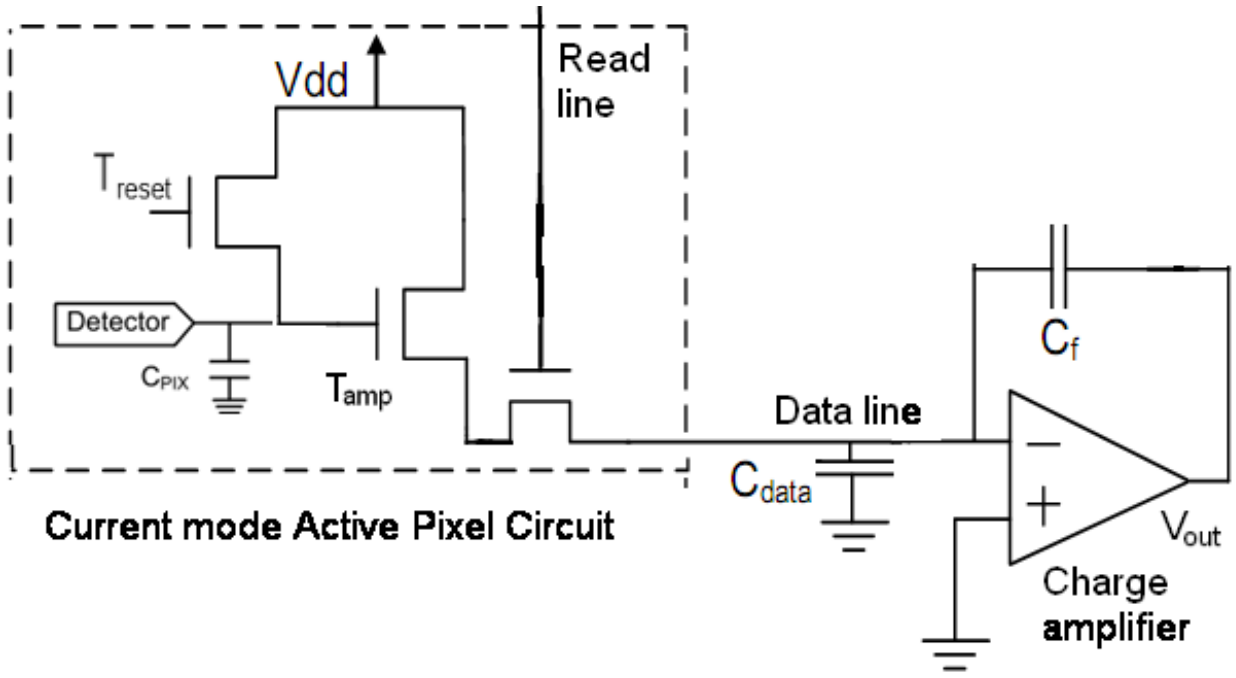

Figure 25 : Current Mode Active Pixel Circuit Schematic

The C-APS circuit operates in three modes controlled by the T_{reset} and read transistor in the circuit. In reset mode, T_{reset} is turned on to raise C_{pix} to a known value, V_{reset}, while the read line is kept low. C_{pix} represents the detector capacitance, gate capacitance of T_{amp}, and source capacitance of T_{reset}.The value of this capacitance forms an RC time constant with the source-drain resistance that must be given time to settle.

Once the value V_{reset} has been reached, the pixel enters integration mode where T_{reset} is turned off and the incoming photocurrent from the detector acts to discharge the stored charge C_{pix} causing the voltage to change by the same relationship described in equation (2.3.

After a specified frame time, t_{int}, the read line is actuated allowing the voltage stored at C_{pix} to cause T_{amp} to pass a current onto the data line capacitance, C_{data}, where this current can be collected and converted to a voltage by a ratio determined by the feedback capacitance, C_f, using a charge amplifier. Due to the non-destructive readout the current can be sampled before the integration period and after the integration period, a technique known as double sampling, and the change in current due to the photo-generation that is read by the charge amplifier can then be extracted as [38]:

$$\Delta i_{out} = \frac{I_t * t_{int}}{R_{ON} * C_{pix}} \left(1 - \frac{1}{\sqrt{1+2*k*R_{ON}*(V_{reset} - V_t)}}\right) \tag{2.10}$$

Where k is the mobility capacitance gain, $u_{eff} * C_{ox,}$ associated with the transistor process. We can see that lower resistance transistors help by providing larger changes in output current in addition to a higher voltage reset value which are crucial to the operation of this circuit. This current is then integrated onto the feedback capacitor, $C_{f,}$ using a charge amplifier that will provide a gain, G, that is equal to [38]:

$$G = \frac{t_{int}}{R_{ON} * C_{pix} * C_f} \left(1 - \frac{1}{\sqrt{1+2*k*R_{ON}*(V_{reset} - V_t)}}\right) \tag{2.11}$$

What is also notable about the gain in the circuit is that it is dependant on the frame time, t_{int}, so that the read limitation of this circuit has no minimum time akin to the RC time constant in the PPS but rather a minimum time associated with the gain needed in each pixel.

Much like the PPS circuit, then, smaller values of both load and pixel capacitance result in higher gains. This is important because it can be shown that the input referred total noise of the C-APS depends on both the gain and pixel capacitances by the relationship:

$$N_t{}^2 = \left(\frac{\sqrt{{V_{out}}^2 * C_{pix} * C_f}}{q * G * t_{int}}\right)^2 \tag{2.12}$$

Where V_{out} is the output voltage as labeled in Figure 25. In the C-APS circuit the noise levels can be designed for as follows:

- increased with increasing pixel or feedback capacitance but is data line load independent, and therefore suited to larger arrays
- decreased by reducing voltage swings,
- Decreased by increasing the gain in exchange for dynamic range
- Decreased by lengthening the frame time, but this also increases gain and loses dynamic range

The current modulation that takes place at the gate of T_{amp} can only remain linear if the amplifier remains in saturation. For this to be ensured, a restriction is placed on the allowable drop on the gate voltage such that:

$$\Delta V_G = \frac{I_{total} * t_{int}}{C_{pix}} \gg (V_{reset} - V_t) \tag{2.13}$$

Where I_{total} consists of the summed photocurrent and dark current of the detector. This has the effect of limiting the integration time, which has the direct consequence of increasing the noise and the dynamic range in high dose modalities. These properties make C-APS circuits suitable for low dose applications where contrast is not achieved through high energy x-rays but not higher dose modalities such as CT scans.

Another limitation occurs with the charge amplification scheme. Due to the presence current sourced signal the amplifier must be designed to ensure that the feedback capacitance, C_f, of the amplifier does not saturate due to the saturated current data passed by T_{amp}. In order to counter this and preserve the large gain associated with a small C_f, a current sink is usually placed at the input of the charge amplifier to eliminate a large portion the DC current signal not associated with the detector. This has the effect, however, of increasing the noise levels of the circuit overall if not designed properly. Otherwise, the charge amplifier in this circuit can be optimized for lower noise performance than in the PPS case because the low input signal constraint has been removed.

2.4.3 Circuit Summary

This section gave a summary of pixel architectures suitable for high speed x-ray imaging. Either of these circuits would fulfill the second stage of imager optimization choices necessary for signal quantification in an imager. Each type of circuit exhibits different noise characteristics and is capable of operating at different speeds. Table 5 summarizes the results

Table 5 : Comparison of Pixel Architectures for Real Time Imaging

	PPS	C-APS
Dynamic Range	Large	Smaller
Gain	Unity	Adjustable
Readout time	$R_{on} * C_t$	Gain dependant
Relative Noise	High	Low
Complexity	Simple	Complex

It was decided that in order to be able to rapidly design and test the array that a PPS design should be chosen. The imager designed in this thesis would be a smaller design so the capacitive loading effect inherent in PPS designs would be avoided. This design still met the minimum requirements for the imager and would offer the quickest turn-around time and past experiences in the STAR research group involving prototyping active pixel circuits into arrays has proven problematic [39].

The PPS array design would also allow for testing to take place on a readout circuit developed in house with the STAR group. The presence of existing expertise and optimization into the readout circuit cannot be underestimated or underutilized and so this is another factor in the selection of a PPS array design.

2.5 Backplane Selection

The backplane of a circuit represents an important aspect of any electronic device, especially imagers. This is because the backplane selection is what determines the circuit properties and process available, sensor size, and vertical integration available with the imager. Two types of backplanes will be analyzed; a common 5um amorphous silicon (a-Si) and the industry standard 0.18um complementary metal oxide semiconductor (CMOS).

Vertical integration describes the ability to integrate and design as much as possible on the sensor backplane itself without having to utilize external discrete components, which reduces the overall price of the imager and can be shown to reduce the noise, increase the readout speed, and give imagers more flexibility [37][40]. Looking at Figure 11, this means translating all the peripheral electronics onto the AMFPI itself. While the concept of vertical integration will play a role in selecting the backplane the design of the vertically integrated components is beyond the scope of this thesis and will not be covered.

2.5.1 Amorphous Silicon Thin Film Transistor Process

Amorphous silicon thin film transistors represent a widely used large area electronic process that has been deployed successfully in areas such as x-ray imaging, document scanning, solar cells, and liquid crystal displays [15]. The success of a-Si in this wide range of applications has to do primarily with the cheap cost, low process temperature, high material flexibility, large area process compatibility, and adequate electrical performance for these areas.

The standard a-Si backplane usually involves a sheet of glass as the substrate on which the thin film transistors are deposited on. The TFT itself includes gate metalization, insulating layers, semiconducting, and the source / drain data lines deposited on top of the glass. The basic a-Si substrate and inverted staggered TFT process is shown in Figure 26.

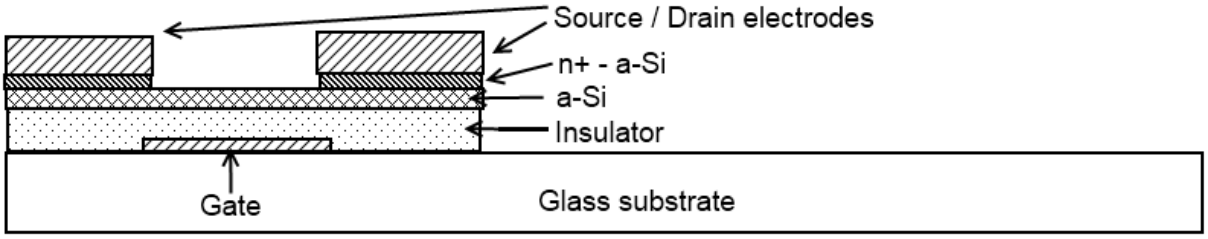

Figure 26 : Typical Inverted Staggered TFT Process

Where the a-Si process falters is that the deposition process allows for only one type of dopant during the fabrication process, depicted in Figure 20, which restricts the resulting circuit varieties, speed, and versatility. Due to the higher electron mobility of a-Si in comparison to hole mobility as seen in Table 3 which restricts applications to NMOS only logic circuits, the relatively large feature sizes of a-Si compared to other technologies, and the larger circuit parasitic capacitances typical cutoff frequencies on the order of 1MHz [41] are feasible on a-Si:H backplanes. While this has been shown to be more than sufficient for the basic readout circuits covered in section 2.4 [15], it is insufficient to provide the gate driving, charge amplifiers, and readout electronics that include correlated double sampling, real time noise filtering and removal, and photon counting can potentially be implemented if the pixel area is reserved for electronics and the detection layer deposited on top.

In addition to this shortcoming, the amorphous nature of this material means that it is a highly resistive material. While this was a good feature for designing the photoconductive layer due to the benefit of low dark current, direct band gap, and low leakage a highly resistive material not only increases noise of the entire circuit based on the equations in section 2.4 but also decreases the speed. Table 6 shows the difference between a CMOS and a-Si:H backplane resistance and speed of a PPS sensor.

Table 6 : Comparison of 0.18um CMOS and a-Si TFT MOSFET parameters

	Parameter					
Technology	k' (nA/V^2)	V_{GS} (V)	V_t (V)	W/L (um)	R_{on} (Ω)	τ_{on} (s)
0.18um CMOS	387000	1.8/3.3	0.5	10 / 5	1k	5n
a-Si TFT	12.5	12 – 15	2	10 / 5	4M	4m

2.5.2 CMOS 0.18um Process

Crystalline silicon (c-Si) represents the scientific and industry standard high speed digitally integrated circuit backplanes in use today [42]. There are many reasons that have contributed to the adoption of c-Si for most general circuit building applications today. Due to the ability to grow well characterizable oxides it is compatible with a variety of physical and chemical patterning processes. Due to defect free crystalline substrates, substrates with large carrier lifetimes and few traps help produce lower noise floor operation. The large wafer sizes compared to the minimum feature sizes that can be patterned on the surface, referred to as the specific *"process node"*, allow for dense systems of circuits that can be made on a single die. Due to the compatibility with a variety of dopants regional conductivity can be tailored to form CMOS circuits This CMOS capability becomes important when you factor in the high carrier mobilities allowing for high speed and complex circuitry that can only be implemented in an economically feasible manner on c-Si today [42].

The fabrication of CMOS circuits is a very detailed and involved process that will not be described here, but will be grouped into two main areas. Firstly, there is the fabrication of the actual c-Si wafer. Wafer growth technology currently produces circular c-Si wafers with a maximum diameter of 300mm which would allow for the minimum panel size requirements listed in Table 2 to be produced on a single wafer. This is important because, unless tiling is used where sensors are stitched together, a c-Si circuit is limited in size to the wafer size. Recently, the price of wafers has plummeted and industry capacity has made the utilization of CMOS electronics in more areas cheaper, and therefore more attractive to engineers [44]. One of the prime motives of this thesis is to take advantage of the drop in CMOS circuit costs to build a cost effective, high speed, low noise x-ray imager.

Secondly in the CMOS circuit manufacturing process is the processing of the wafer. In this stage the wafer is cleaned, doped, metalized, and passivated to form the circuits specified in photolithographic masks. This fabrication process involves high temperatures, in excess of 600°, and is largely automated from start to finish. The steady process research, process refinement, process improvement, and process experience with c-Si wafers has made defect rates plummet and the costs of the wafer itself less of a factor now than they have ever been before. This has led to higher overall yields and less variations when using slightly older and more developed process nodes [45].

For most large area cases the TFT process cannot be replaced. However, with lower c-Si costs and increased wafer sizes the ability to make an imager of sufficient size becomes attractive. Table 7 summarizes the two processes considered as backplanes for this circuit.

Table 7 : Comparison of Substrate Technologies

	CMOS	TFT
Circuit Area	21cm x 21cm	>100cm x 100cm
Cost	Higher	Low
Circuit Complexity	High (CMOS)	Low (NMOS only)
Circuit Speed	> 1GHz	~1MHz
Feature size	0.18um	5um

When the choice of substrate was considered the novelty of integrating an amorphous semiconductor with a high speed crystalline substrate was decided upon. This would allow for pixels to be built with near 100% fill factor while retaining the high speed and low noise operation of the imager. The imager size could also be made sufficiently large while the components that make a digital imaging system shown in Figure 11 could be developed and deployed on the same substrate

2.6 Summary

This section has given an overview only the system overview and design considerations of building a large x-ray imaging device. We have discussed the merits of indirect conversion that reduces design and integration concerns. Then, a discussion on how amorphous photoconductors can be used to give large area uniform photo response resulted in optimum thicknesses for absorbing the light emitted by a CsI:Ti scintillator.

Two main imaging circuit architectures and two main circuit substrates were detailed and compared for their speed, noise performance, and ease of design and integration. This resulted the choice of a PPS sensor array on a CMOS process as a new type of imager design that would allow for sufficient speed and low noise for tomosynthesis.

Chapter 3
Design of an 8x8 array

This section goes through the design and simulation of an 8x8 array of pixels on a 0.18um CMOS process. Considerations and compromises are detailed in relation to meeting the minimum requirements established for the active matrix imager earlier. Issues in design and fabrication are also discussed along with the methods used to accommodate the CMOS substrate with the amorphous photoconductor. Finally, the finished array is qualitatively assessed before testing.

3.1 Process Considerations

Before detailing the actual design of the array it is important to discuss the tools, environment, and process that were used. These are important factors as they determine some of the limitations in trying to integrate the photoconductor with the substrate.

The 0.18um CMOS process from TSMC was a given as this was the process that was available to the STAR group during the implementation of this idea. This process comes with properties that are fixed and so must be accounted for. The actual design documents that detail most of these limitations are supplied confidentially and so cannot be attached or shown but they can be discussed.

An example of a limitation for the 0.18um process is the 1.8V maximum that can be applied between any two parallel conductors before the dielectric between them breaks down. Although there is a high voltage (HV) process available that allows for voltage levels up to 50V, it was not used.

When any of these fixed process parameters are encountered they will be mentioned and alternatives that are available to improve the design will be mentioned and discussed further in 0.

3.2 Lateral Pixel Considerations

In Table 2 the minimum pixel size for mammography and CT scanners was given as 50um and 80um. In order to meet both of these requirements at the same time pixel binning can be used if certain criteria are met. To do this you need to design for the lowest pixel size requirement. If larger pixels are desired for a different modality or lower noise then they can be formed by addressing groups of pixels in a PPS system and the charge for each pixel will be read in sum and averaged as the reading for one pixel when read out. A diagram of this can be seen in Figure 27 demonstrating the tradeoff.

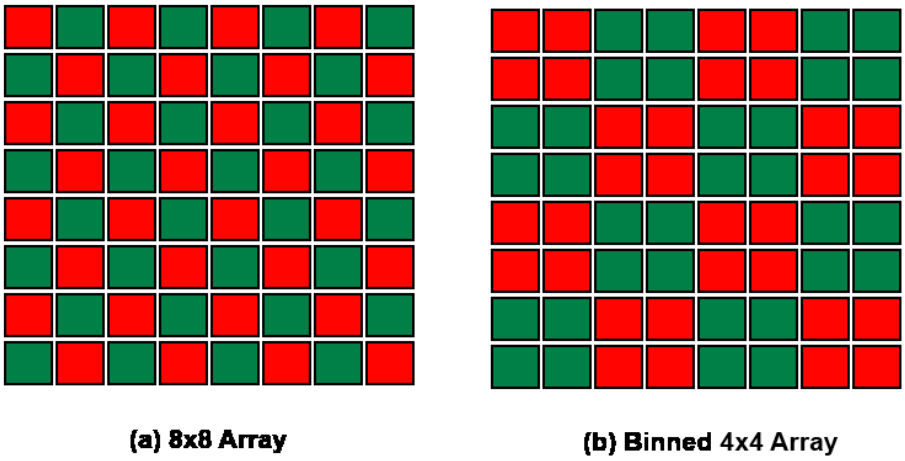

Figure 27 : Example of (a) high resolution array and (b) pixel binned array

This let the minimum pixel size be set to half of the largest one, 40um. This 40um pixel size is much larger than the calculated electron and hole range calculated for both a-Se and a-Si:H listed in table Table 3, so to minimize the recombination of carriers and maximize the photo-response. To solve this problem the lateral electrodes on the surface should be combed so that the distance between them is less than the minimum electrical length, 4um.

This value of 4um conflicted with the safe step coverage size for a-Se evaporation in the G2N lab. The top metal layer, which is where the photoconductor would be deposited, has a metal height of 1um. With only 2um of a-Se to be deposited on top the aspect ratio was lower than was considered safe to avoid crystallization and ensure good contact with the metal at both electrodes. Most deposition lab work had gone to vertical detectors which don't have step coverage issues and there was no established minimum value that had been established. Instead, a safe value was set instead at 8um. After inclusion of a guard ring to reduce pixel crosstalk and dark current [46] the final pixel structure is as depicted in Figure 28 which shows the drain for the pass transistor, the cathode biasing electrodes, and the anode collecting electrodes.

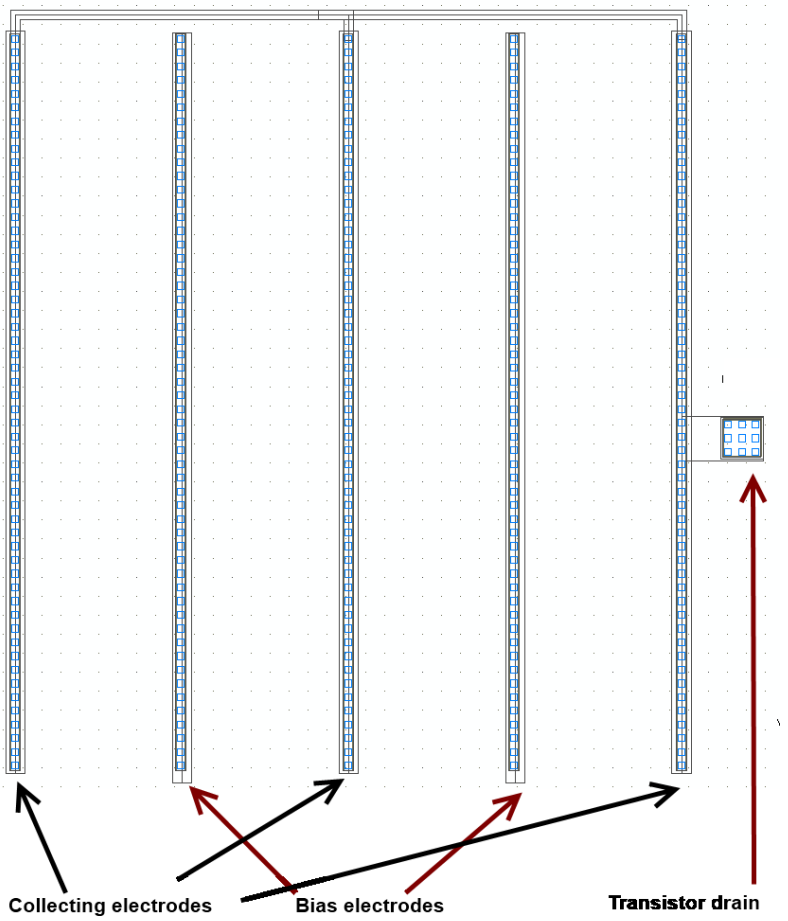

Figure 28 : Enhanced CMOS micrograph of lateral electrodes in a pixel

To ensure that the electric field was uniform throughout the structure, which aids in achieving a uniform photo-response for any absorbed photon in the pixel, Centaurus Medici was used to simulate the electric field weighting potential for the lateral electrodes with a-Se deposited on top. The result can be seen in Figure 29. The e-field distribution remains fairly constant with only minor fringing on top of the electrodes indicating that the pixel should run into few non-uniform response issues for any photons absorbed at the top or at the edges of the electrodes.

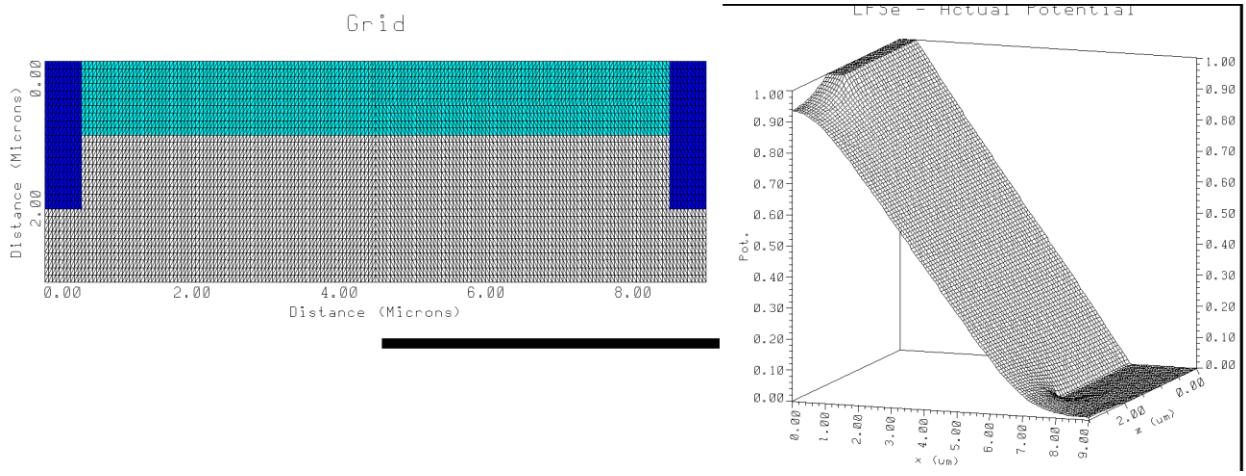

Figure 29 : Medici E-Field Simulations for Lateral Pixel Electrodes

3.3 PPS Array Considerations

The passive transistor was designed to meet the minimum timing resolution of the readout board of 20ns minimum. The readout board is developed and detailed in the work of a previous group member [36] and can be seen in Figure 30. This readout board demonstrates the complex circuitry required to drive a PPS array and is a motivation to use a c-Si substrate as all the components on this board are able to be implemented on the CMOS process itself.

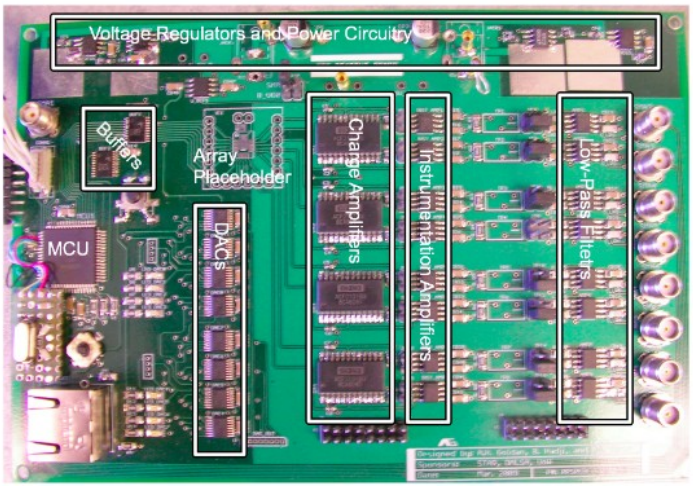

Figure 30 : Original PPS Readout Array Electronics [36]

When the load capacitance of the 8 readout metal lines and charge feedback amplifier are considered a transistor width and length of 10um by 5um was simulated to be sufficient.

In order to implement the 1pF capacitance required due to the low a-Se intrinsic capacitance and a small parasitic capacitance on such a small pass transistor it was necessary to utilize the metal layers available in the 0.18um CMOS process. This was done for two reasons. Firstly, the usual capacitor layer, called MIMCAP, designed for building capacitors was not available because it had to be utilized in order to provide the routing for the bias electrodes in the lateral pixel. Secondly, if on chip circuits are to be implemented then the silicon substrate should be kept relatively bare to leave room for those future circuits.

The approximated complexity for circuits that can be implemented in a 40um x 40um pixel can be calculated to roughly require only two layers for most routing [47]. This led to fingered capacitors being implemented on metal layers 2, 3, and 4 which would leave the poly layer and metal layer 1 open to perform routing for any CMOS electronics below. A diagram of this can be seen in Figure 31 along with the micrograph of the pixel cell when completed.

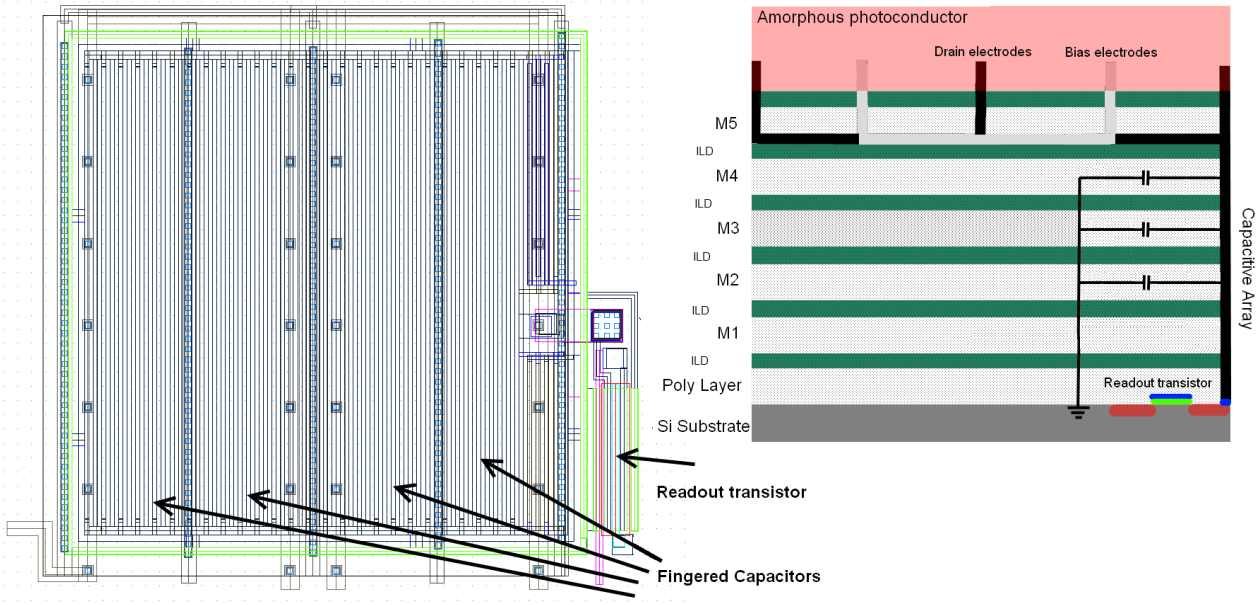

Figure 31 : (left) Micrograph and (right) diagram of pixel routing and capacitor design

The capacitance was simulated by extracting the parasitic of the fingered metal lines in Cadence using supplied models for the 0.18um process and found to be 0.977pF, sufficient for a-Se imaging.

The imager was then formed by tiling the pixels 64 times in a column and row fashion to get an 8x8 array of pixels. This was easy to accomplish because each pixel was designed with routing in and routing out methods for both the gate and drains of the transistor, along with a daisy chain routing structure for the biasing electrodes. This means that while all pixels share a common biasing connection for the whole array they each contain two biasing electrodes per pixel. The final array structure can be seen in Figure 32.

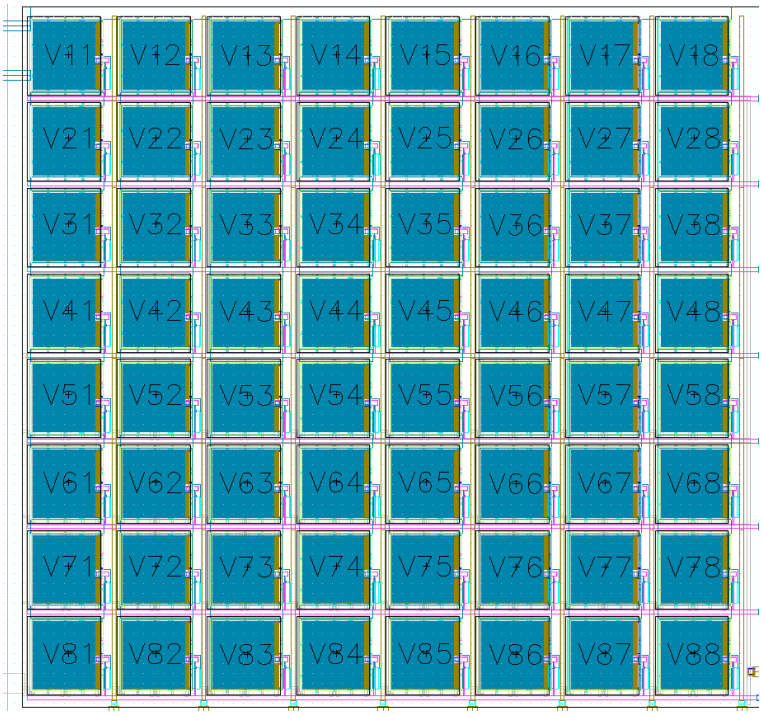

Figure 32 : 8x8 Array arrangment with internal pixel routing

The top metal layer had a ground-able guard ring designed to surround the array. This array guard ring is designed to reduce the external noise and potential interference from any absorbed photons that occur outside the array itself. The pixels were then routed to bond-pads designed to make the PPS array compatible with the previous read electronics. The bonding pads needed for this array are 8 gate lines, 8 readout lines, a bias pad, a guard ring bias pad, and two ground pads. A final micrograph of the entire chip can be seen in Figure 33.

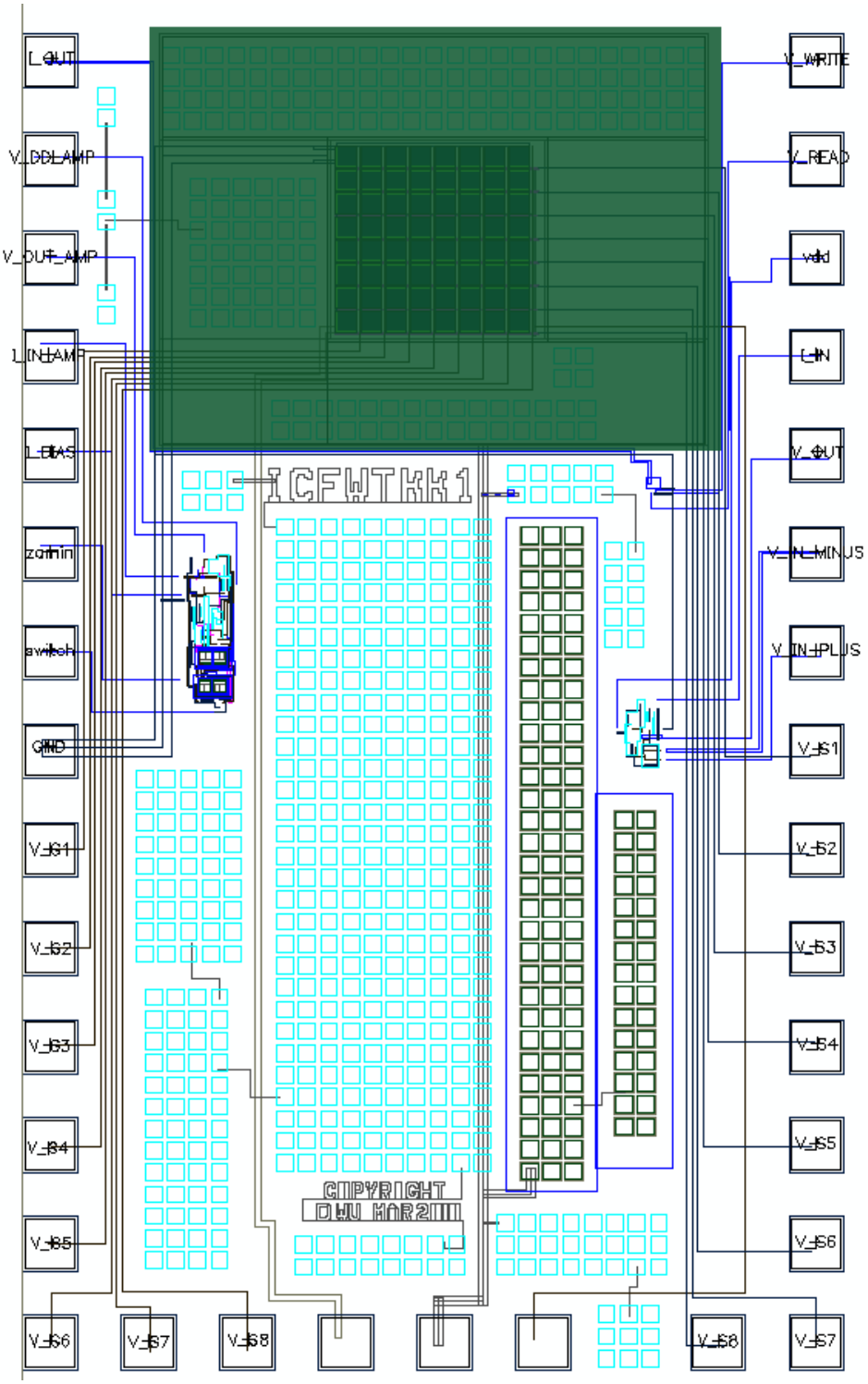

Figure 33 : Micrograph of final 8x8 array chip with bondpads

3.4 Issues in fabrication

In order to deposit the photoconductor on the top of the array the passivation layers deposited during fabrication have to be omitted. In Figure 33 the area at the top of the area shaded in green represents the area to be omitted from the passivation process.

When an area is omitted it is still subjected to the remainder of the fabrication process, however. For the final few hours in the 0.18um TSMC process this means that the substrate is annealed in an oven at 600°C which has the effect of stabilizing the electrical and mechanical properties of a normal device. Without the passivation layer to protect the top layers, however, any exposed layers are subject to heat induced stress and strain which has a particularly large effect on small, thin runs of metals like the biasing and collecting electrodes in the lateral pixel design.

In order to combat this effect known as thermal peeling, multiple vias were put underneath the electrodes to try and anchor them firmly into place. This also prevents from a single electrode, which is daisy chained in the case of the bias electrodes, from peeling off and disabling the entire row of pixels because routing is maintained underneath the top layer between pixels at all times. This did not have the effect of fully stopping some of the electrodes from peeling off, however. When viewed under an optical microscope the exposed array looks like that seen in Figure 34. Initially it can be difficult to spot if thin metal electrode layers have peeled off or even what effect the peeling may have on the integrity of the array.

To examine the detrimental effect of peeling samples of chips were analyzed using a SEM and high powered optical microscope available at the G2N lab. The array results can be observed in Figure 35 and seen to occur across the chip at random locations. When viewed under an SEM the defects are much clearer and easier to spot, revealing that some of the electrodes of both the bias and collector portions have been peeled off.

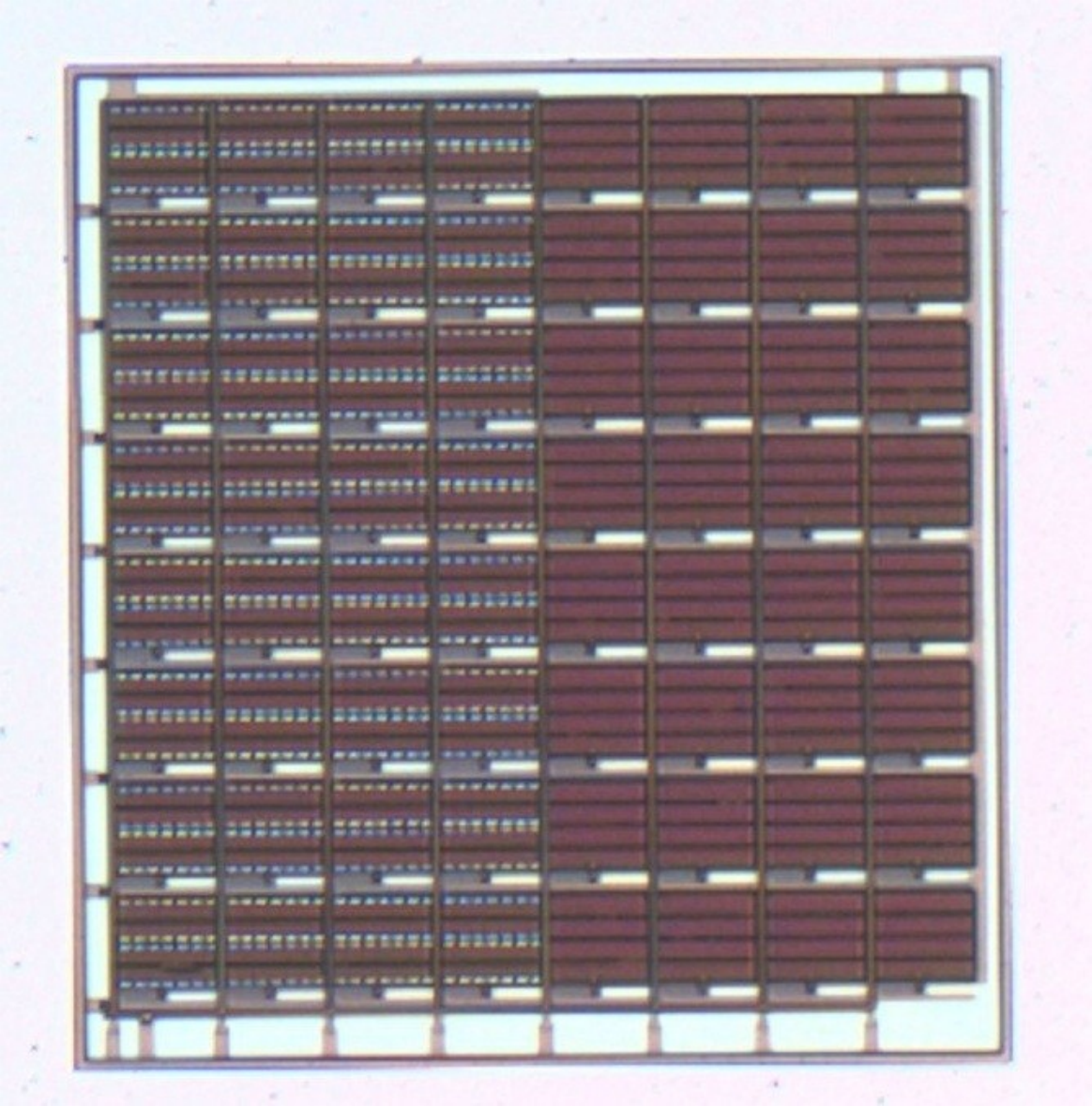

Figure 34 : Optical Microscope Zoom of Active Pixel Area

The peeling of an electrode has the effect of introducing non-uniform electric field distribution in the pixel and reducing the effective fill factor of the pixel but, due to the vias and routing underneath the peeled electrode, should not actually result in a dead pixel itself. There is no way to observe or account for the peeled electrodes other than with visual inspection before and after deposition, so this factor must be accounted for in future revisions and will be discussed in 5.3.

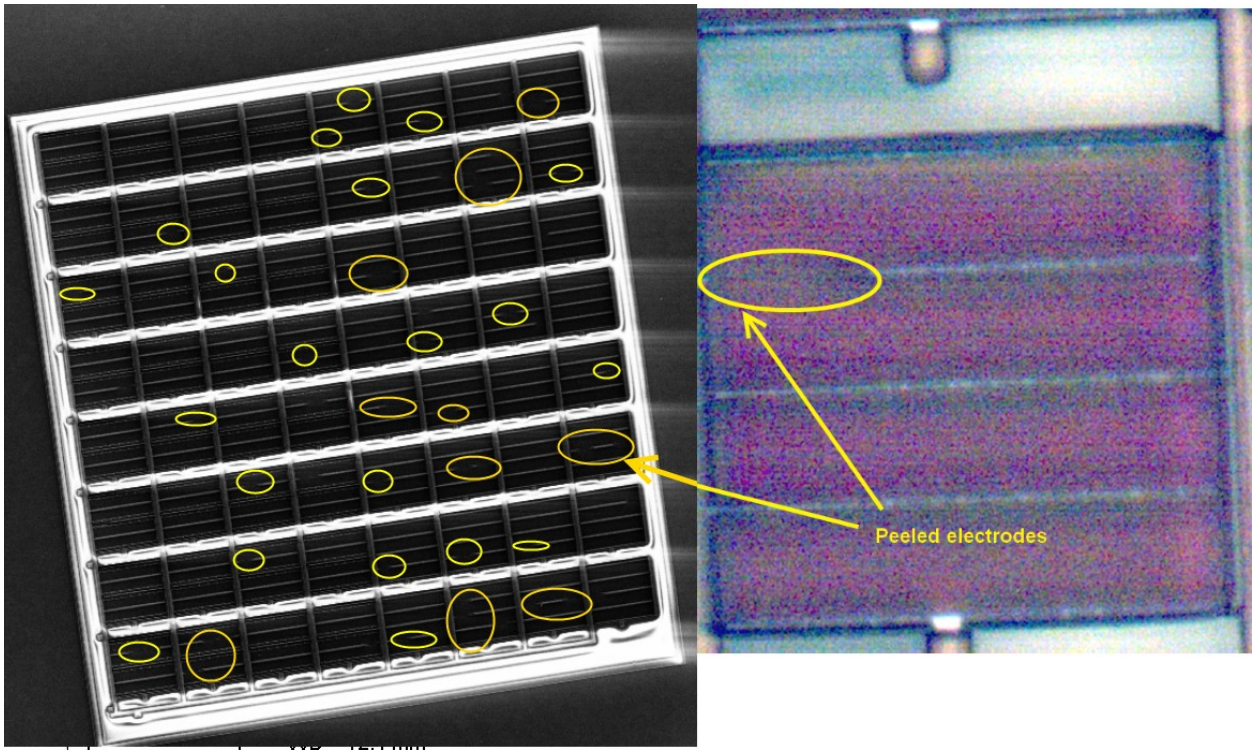

Figure 35 : (left) SEM and (right) Optical image of array electrode peeling

3.5 Issues in Photoconductor Integration and Chip Handling

In addition to the issues encountered during the tape out and fabrication of the substrate there are issues that warrant discussion related to the deposition of the amorphous photoconductor. As mentioned in sections 2.2.4 and 2.2.5, both a-Se and a-Si:H are deposited using different mechanisms, thermal evaporation and PECVD respectively. Either of these steps represents a further point of contamination or failure in the production of the detector.

The dangers in the evaporative process are crystallization of the a-Se and the handling of the chip. Crystallization has been discussed previously in 2.2.4 and so will not be covered here. Figure 36 demonstrates what the 2um a-Se deposition looks like before and after crystallization on a CMOS die.

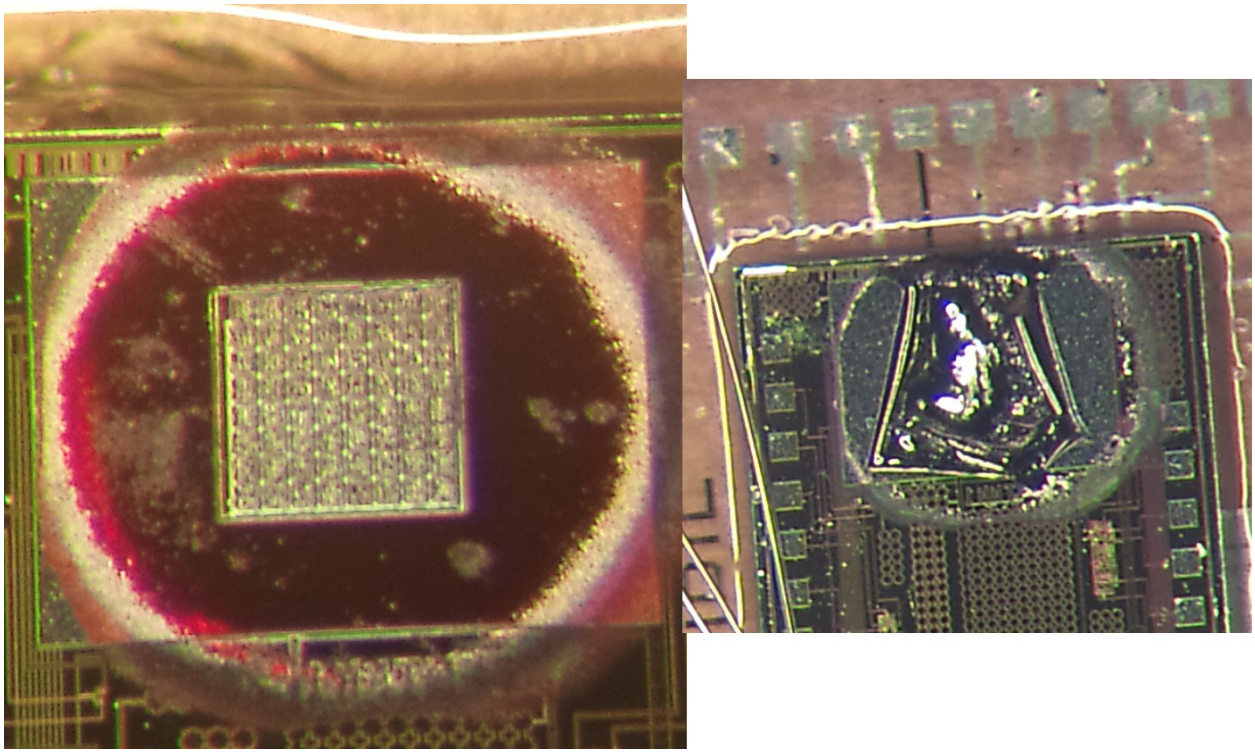

Figure 36 : (left) Amorphous vs (right) Crystallized 2um Layer of a-Se

The input gates of the PPS array was not designed with electro-static discharge (ESD) protection in mind and this was a major oversight and barrier that will be discussed further in Chapter 4 and 0. In essence, handling of the electronics by inexperienced or personnel that are not careful with maintaining proper grounding for their bodies and clean-room procedures can expose the bond pads of the chip to voltages as high as 10,000 V without the user being aware of anything [48].

In the PPS circuit of Figure 24 this causes the extremely high voltage to be applied to the gate or source of the pass transistor. With no other diode like structures or methods of discharging elsewhere, this extremely high voltage burns through the gate oxide and effective destroys the oxide creating a short circuit through the gate to the source and drain of the transistor, which is irreversible. After this has happened it's possible that all of the 8 gates connected to that bond pad have been destroyed and so the entire row of pixels is effectively dead. This happened to a fair amount of test chips in which a-Se was deposited and proved a major issue in trying to get a working array.

For a-Si:H the dangers are due to two different sources of ESD. The handling of the chip still remains a potential point of failure in the gates due to ESD shock but there is also a new ESD source, the PECVD chamber used for the deposition. The PECVD chamber using an RF power source that can potentially resonate with metal electrodes in the circuit that happen to be properly shaped, exposed, and un-grounded. This can cause a large voltage to build up on the metal trace, referred to as the antenna effect, which can cause the same dielectric breakdown seen in the gates [49], but this time localized to the fingered capacitors that were implemented on metal layers 2, 3, and 4 which were connected to the collecting electrode exposed on the top surface.

The last ESD issue involves dielectric breakdown caused by errant operation of the chip. In the PPS structure the dark current integrates onto C_{pix} to create a voltage at the drain node of the pass transistor, V_{pix}. If the cathode is biased higher than 1.8V than V_{pix} can build up past the safe limit for the source-drain-gate present in the 0.18um CMOS process and break down the dielectric. Using the relationship between collected charge due to total current, I_t, and the maximum allowed safe voltage of the process, V_{max}, the maximum time that a PPS sensor can be left without being reset can be calculated as:

$$V_{pix} = \frac{\mathrm{Q}}{Cpix} = \frac{I_t * t_{int}}{Cpix} \rightarrow t_{int} = \frac{C_{pix} * V_{pix}}{I_t} \tag{3.1}$$

Based on the expected total current in the sensor the integration time should be selected accordingly to avoid potential breakdown in any PPS pixel.

The next issue encountered with the a-Si:H integration was the non-uniform deposition that results in subtle bumps, defects, and variable thickness in the resulting photoconductive layer. This can be seen in Figure 37 which shows the speckles due to particle contamination and the thickness gradient which can be seen by the change in colour due to the different absorption depths that results in colour selectivity.

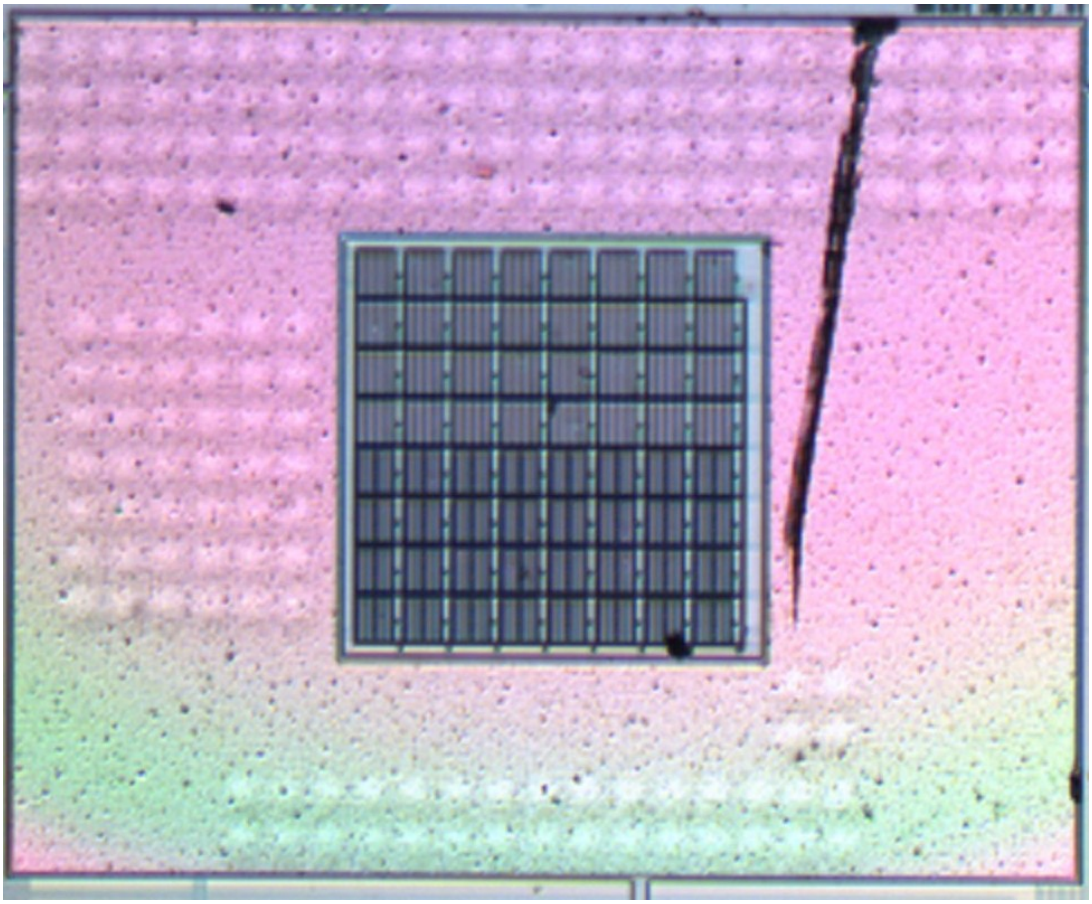

Figure 37 : Array Coated in ~500nm of a-Si:H Showing Non-uniform Deposition

This was due to the lack of a standard set of masks for the chip for use in the PECVD chamber. Masks were fashioned from old silicon wafers that had been bored out to provide a proper opening for the deposition but did not guarantee that the sample substrate was flat itself. The non-uniform deposition will manifest itself as a change in a pixel's response to certain wavelengths of light, effectively reducing the total photo-response. This will not be an issue of the loss of response is outside the scintillating film's spectral output.

3.6 Modifications to Test Read Board

During the fabrication and troubleshooting of the detector circuit the readout electronics that would be used to drive the PPS transistors and provide the charge amplifier readout were unable to be finished. Due to this setback an adapter was made that allowed for the imager to be tested from a standard DIP package.

Although this would not allow for real time image readout as originally planned, it would allow for the rows and columns to be addressed which would allow for pixel readout using standard lab test bench equipment such as DC power supplies, function generators, and an oscilloscope for the output. The adapter consists of a voltage step down converter so that the PPS transistors can be driven by common 5V MC14007 digital logic inverters, accessible bias and ground wires, and short source readout wires to minimize parasitic capacitances all on a low noise Vector Proto-PCB. The DIP adapter can be seen in Figure 38.

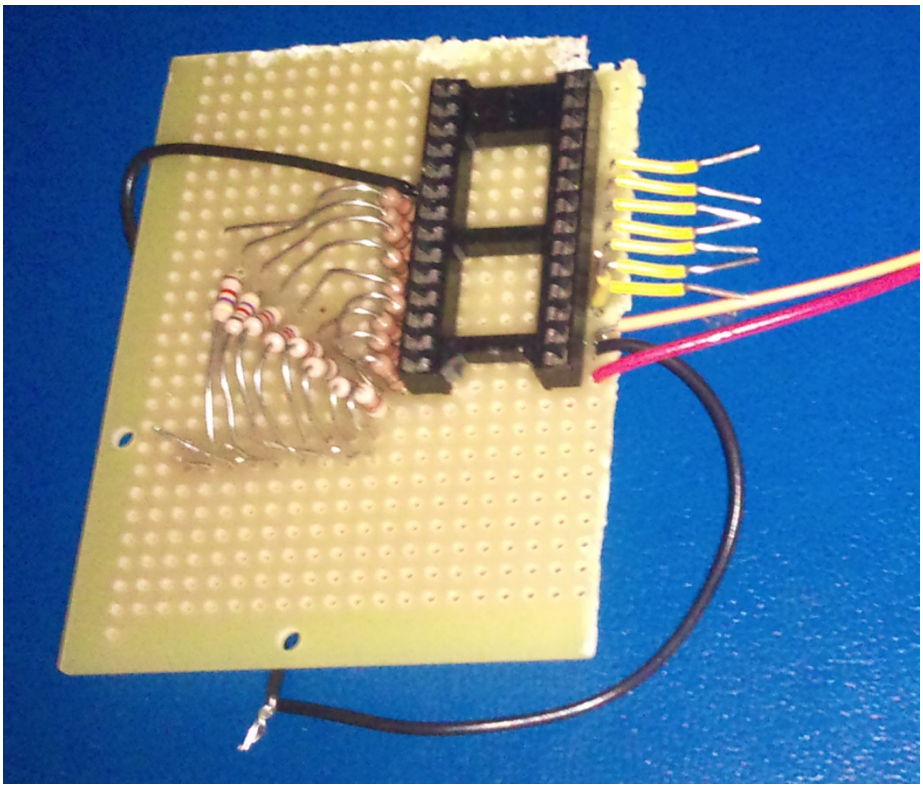

Figure 38 : DIP Adapter for Modified Readout Circuit

3.7 Summary

This section has detailed the designs and modifications required to fabricate a photodetector and interface a 0.18um CMOS process to a lateral structured amorphous photoconductor. Issues with the circuit fabrication, post-processing deposition, and readout circuits have been detailed. The final design specifications of the array can be summarized in Table 8.

Table 8 : Final Array Properties

Criteria	Designed Value
Array size	8 x 8
Pixel size	40 umx40um
Drive / Readout	PPS (externally controlled)
Max Voltage	1.8V
ESD Protection	None
C_{pix}	0.977 pF
Fill Factor	79.6%
Detector Thickness	2um (a-Se) 625nm (a-Si:H)

Chapter 4
Testing

This section will detail the methods and results used to characterize the fabricated chip. First, PPS functionality will be verified using DC IV curves and C-V measurements. Finally, the photo-response of a pixel will be tested using QE measurements.

4.1 PPS Functionality

The PPS cell depicted in Figure 31 represents a compromise between trying to fit a topside photoconductor onto a standard 0.18um CMOS process. In order to verify that these compromises have been met with acceptable trade-offs the implemented cell must be characterized. To do this current, voltage, and capacitance relationships must be extracted from a test chip that has had the array shorted with conductive paste. Once this is done the chip is mounted onto a DIP package and wire bonded so that the bond pads can be used to turn the pass transistor into a basic three terminal device. Figure 39 shows a photo of a device that has had the array portion shorted with silver paste.

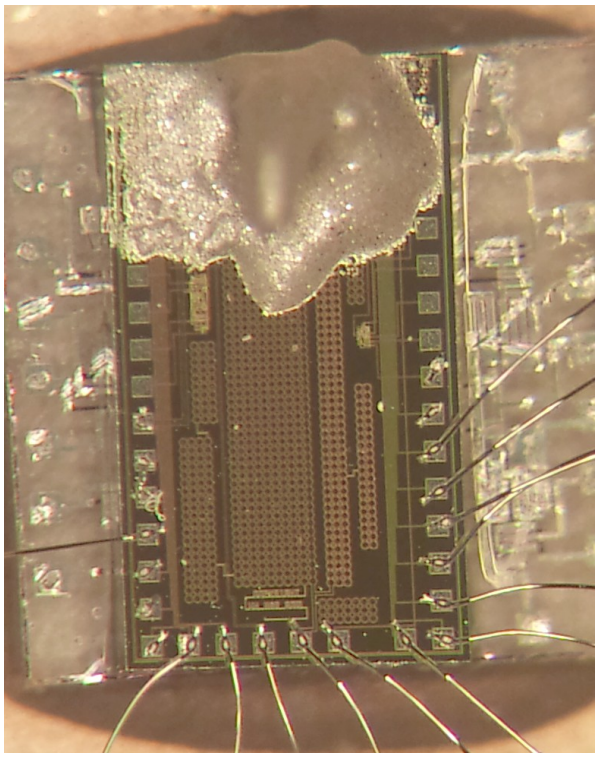

Figure 39 : Silver Paste Shorted PPS Array

Once this has been done the chip was carefully subjected to DC testing. This has the effect of permanently destroying the test chip. When combined with the ESD issues discussed in 3.5

4.1.1 Transistor Performance

To test the transistor performance two tests were performed. First, the capacitive well could be tested to ensure the storage capacitor was around 1pF. This was done using an RC time constant method. 1.8V was applied to the gate pad of a column of pixels and a 1MΩ resistor was placed in series with one of the source pads. Using an active probe with known loading the rise time response was measured to a square wave input of 5KHz 1.8V peak to peak.

The capacitance of the cables and package were measured separately and subtracted to account for setup parasitics The capacitance of the selected source column includes every pixel in the row, however, so 8 pixels were measured at a time and the measurements were averaged before being divided by 8. A value of 1.243pF was calculated. This value is larger than the original design value 0.977pF and so represents an overcompensation

The next test involved getting IV curves from the device. For these measurements the device was connected to an HP4156 and the Agilent 16422 test Fixture as shown in Figure 40.

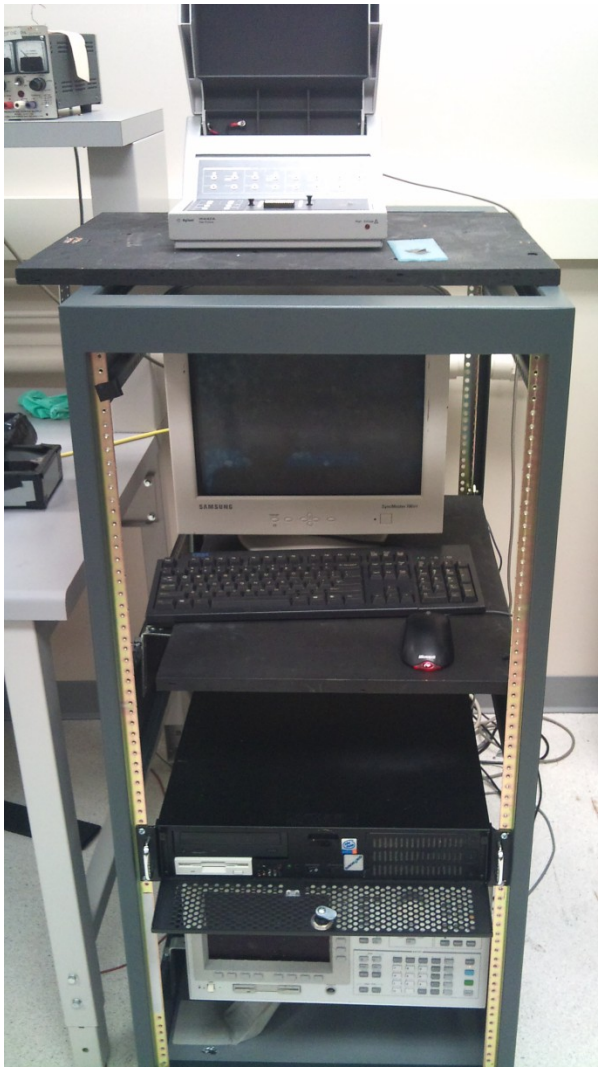

Figure 40 : HP 4156 Parameter Analyzer

To obtain the saturation MOSFET curves a single transistor was swept from 0 to 1.8V at increasing steps of 0.2V on the gate. The results of these curves can be seen in Figure 41.

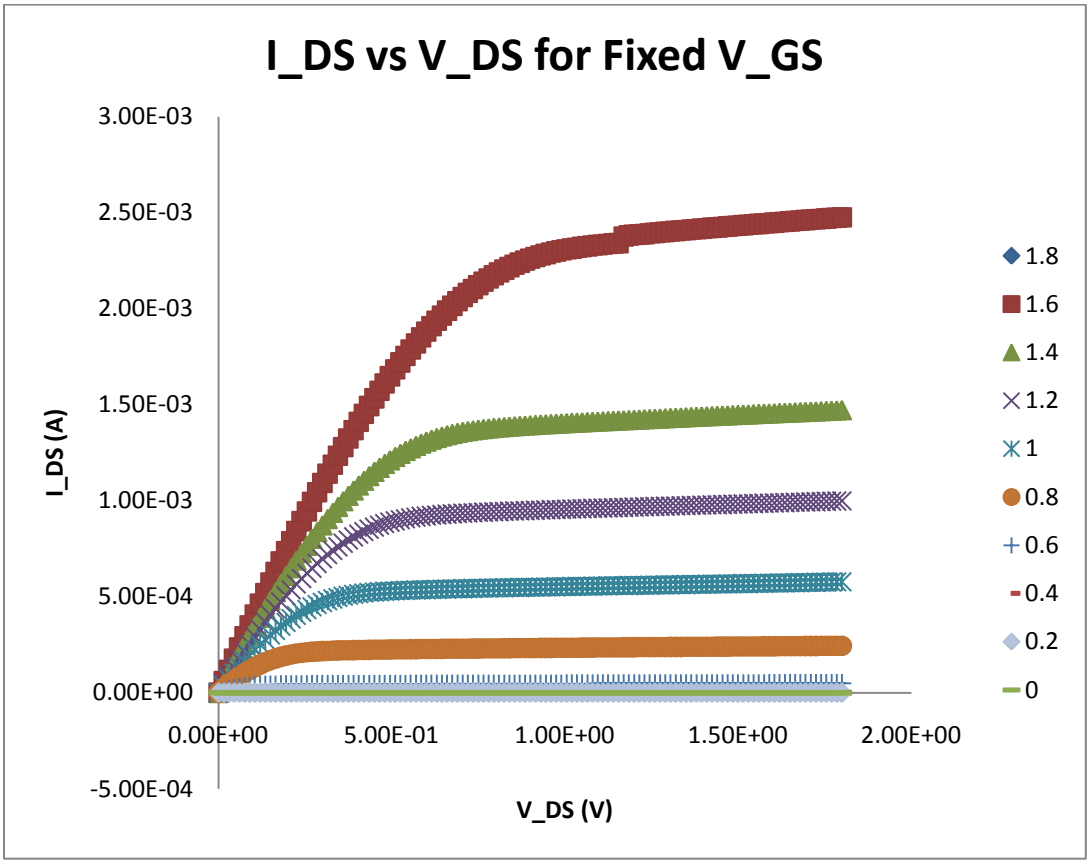

Figure 41 : Ids vs Vds for various Vgs of PPS Transistor

We can extract a saturation current of 2.5mA and a linear region R_{on} of 300Ω and a saturation region R_{on} of 727 Ω. This represents a lower on resistance than previously predicted and will serve to decrease the readout noise of the device and increase the speed. To extract the leakage and threshold values of the transistor Vds was swept while Vgs remained constant. The drain current of the transistor was measured and the results of this can be seen in Figure 42.

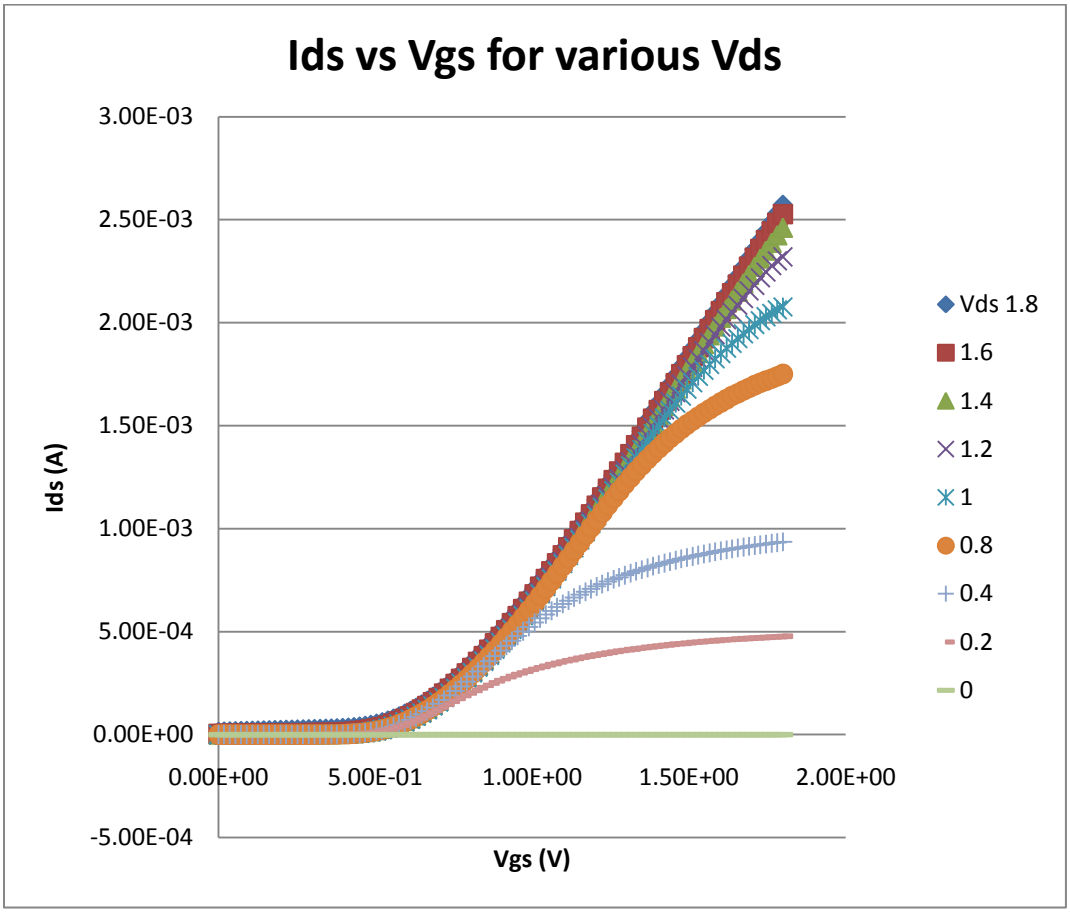

Figure 42 : Ids vs Vgs for Various Vds of PPS Transistor

From this graph the threshold voltage of the transistors can be seen to be ~0.6V, which is higher than for the 0.18um CMOS process. This could be attributed to the high resistance of the silver paste that was used which would effect the effective voltage drop across the transistor contaminating this measurement. The effective mobility was also extracted from this graph to be 1100mA/V^2. For the purpose of a PPS sensor which acts a digital switch this is sufficient.

The full bias leakage, where Vds is 1.8V and Vgs was set to zero gave an off current of 11.3uA, resulting in an on / off ratio of 22750. This leakage current is higher than reported for a-Si:H transistors which are in the order of nA when voltages this low are being applied [15]. If a high dark current exists than this leakage value will serve to increase the total noise of the circuit and degrade the readout image.

4.2 Effective Quantum Efficiency

The Effective Quantum efficiency (EQE) is a measure of a device's ability to detect incident photons which includes absorption and readout. This is in contrast to just the quantum efficiency (QE) which is simply a function of absorption depth for a given wavelength which describes the ability of a material to generate a e-h pair for an absorbed photon which has, in effect, already been designed for by targeting a specific absorption depth for the photoconductive material. A higher EQE will be directly correlated to an imager's ability to generate a larger SNR. EQE is a ratio of detected photons to incident photons and so, in the absence of gain, will be less than one. The EQE of both a-Si:H [50] and a-Se is known to be a function of the bias applied across the photoconductor because this determines the ability to separate the charged carriers created in an absorption event. The EQE was calculated using the formula [51]:

$$\mathrm{EQE} = \frac{\mathrm{I_{photo}} * \mathrm{h} * \mathrm{c_o}}{P_i * A * \lambda * e} \tag{4.1}$$

Where I_{photo} is the photocurrent, h is Plank's constant, c_o the speed of light in a vacuum, λ the wavelength of light, e the charge of an electron, P_i the incident power per unit area and A the unit area. To maximize the EQE then the only factor in a detector is to increase the photo-current. In a PPS sensor with no gain, this can be accomplished by minimizing recombinations and maximizing absorbtion.

To measure the EQE a Jovin & Yyves H1010 monochromator was setup and calibrated to sweep through a range of frequencies for a set period of time. The output power of the monochromator determines the density of incident photons which represents the signal level. The imager had a single source bond pad connected to an HP4156 inside an Keithley 8008 text fixture. Light was then directed onto the device for a period of time while the current was measured. The dark current was measured and subtracted from the measured current to get the photocurrent. The electrode biases were varied to see if they had any effect on the efficiency. A setup of the test bench can be seen in Figure 43. The samples were given two minutes to rest between measurements in which the source and bias electrodes were shorted while light was still incident on the sample. This is to reduce the effect of traps and stress that are inherent in amorphous semiconductors.

Figure 43 : EQE Setup

An issue when running this test is that the biases were limited to voltages that are unable to provide high electric fields across the photoconductor for efficient collection. Also, both these materials are capable of a phenomena called avalanche gain when biased sufficiently high that was not able to be used which is capable of providing EQE of greater than one. This was due to the dielectric breakdown between the routing layers of the high voltage metal lines, collection lines, and other routing done on the chip. The lack of blocking contacts also leads to higher dark currents than is preferred.

The amorphous selenium EQE measurements can be seen in Figure 44.

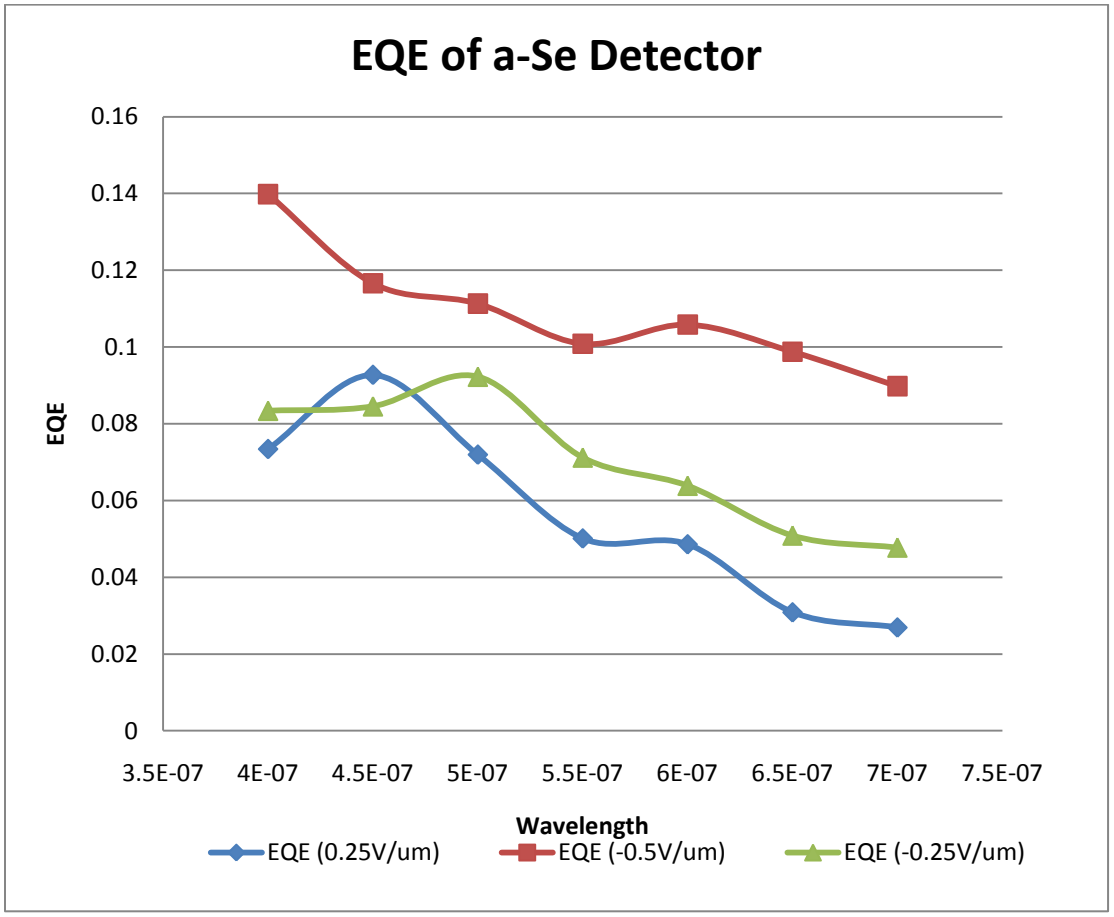

Figure 44 : EQE of a-Se Detector

We can see that the EQE results depend on bias, with negative biases, or the collection of holes at the bias electrode, yields a higher EQE. The peak EQE at -0.5V/um bias is 27.9% and the EQE at 550nm, which is the peak emission of the CsI:Ti scintillator, is 10%.

Based on the EQE at 550nm and the dark current present at a specific bias, contrast ratios and maximum frame times can be calculated which determine the dynamic range of the imaging array, or the greatest difference between no detected photons and the maximum that can be stored on C_{pix} safely using (2.3. The -0.5V/um case of a-Se this yields a frame time of 1.3s, showcasing the low dark current which makes a-Se an attractive photoconductor. The contrast ratio of if using imager at 30Hz, or for a frame time of 33ms, is 1.22.

The results of the test on an a-Si:H sample are graphed in Figure 45 at the 4 biases tested.

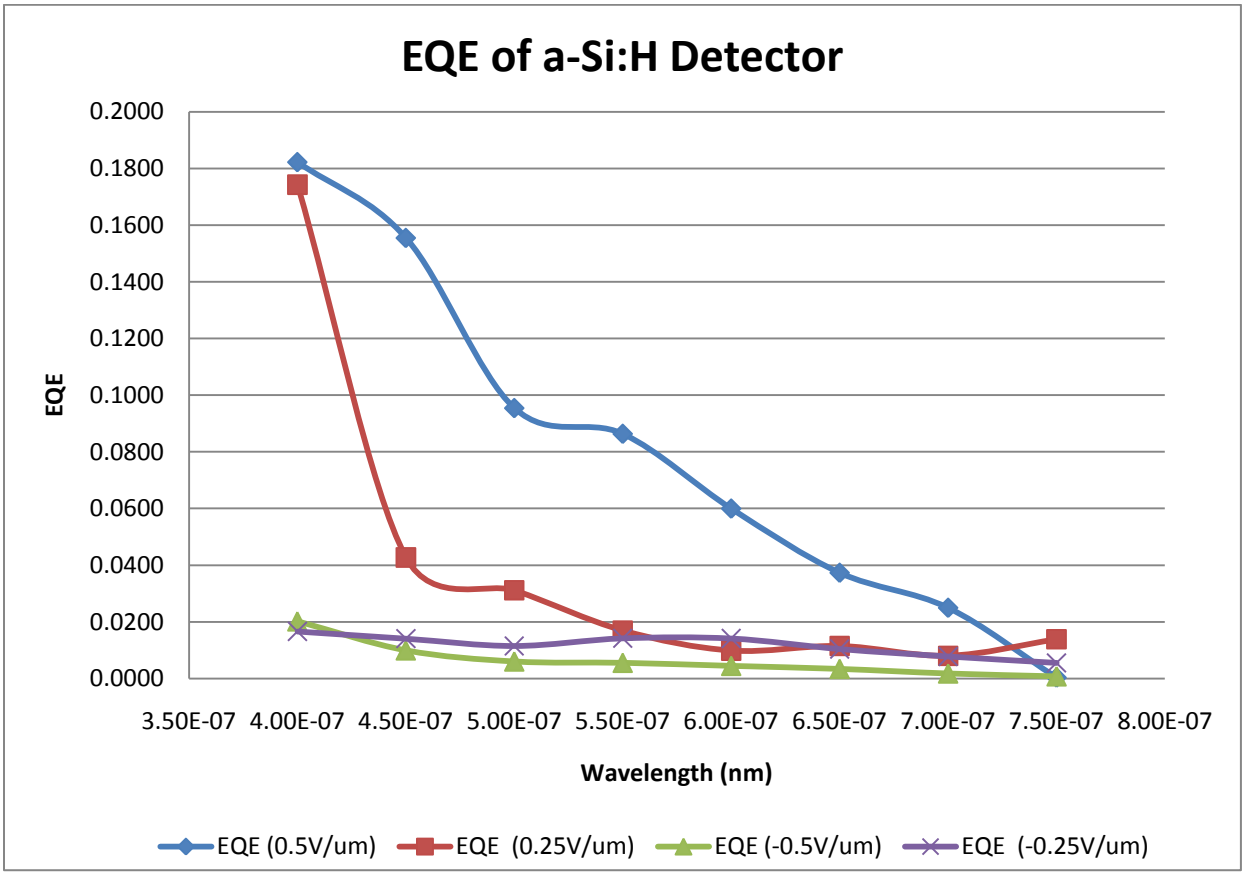

Figure 45 : EQE of a-Si:H Detector

Again we can see that the EQE results depend on bias but this time with positive biases, or the collection of electrons at the bias electrode, yields much higher EQE. This is due to the electron mobility which is significantly higher in a-Si:H than the hole mobility, as shown in Table 3. The peak EQE at a 0.5V/um bias is 18.2% and the EQE for 550nm is 8.6%.

The 0.5V/um case of a-Si:H this yields a frame time of 57ms which is sufficient for real time applications such as fluoroscopy [15]. The contrast ratio of if using imager at 30Hz, or for a frame time of 33ms, is 1.96.

4.3 Transistor Noise Performance

The noise performance of the transistor was measured and calculated based on the equation 2.9. For the thermal dataline noise a single pixel was hooked up to an Agilent 4952 Spectrum analyzer and a Perkin Elmer 5182 ultra low noise amplifier. The thermal noise was measured and averaged for 1024 readings over 1 hour in an isolated Faraday cage with the PPS transistor both on and off for separate readings.

In order to generate values in terms of electrons the following formula was used:

$$q_T^{\,2} = \frac{k*T*C_{pix}}{q_e^{\,2}} + \frac{I_{dark}*T_{\text{int}}}{q_e} + \frac{I_{photo}*T_{\text{int}}}{q_e} + \frac{\pi*k*T*C_d^{\,2}}{2*q_e^{\,2}} \tag{4.2}$$

Where the first term accounts for the reset noise, the second term accounts for the dark current shot noise taken from the EQE testing, the third term accounts for the photocurrent shot noise taken from the 500nm EQE test, and the last term accounts for the thermal noise that was measured. The noise values are then added in quadrature and the square root of this value is the RMS noise contribution of the imager to the final output value.

For the a-Si:H detector the RMS noise value was 1280 electrons and for the a-Se detector it was 700 electrons. The large discrepancy has to do with the much larger dark current present in the a-Si:H. The limiting factor for the noise in this circuit was the reset noise, which accounts for 420 electrons RMS itself. The noise voltage per pixel can be found from equation 2.3 and is equivalent to 90.2 uV for the a-Se detector and 165 uV for the a-Si:H detector.

4.4 Summary

This chapter has detailed methods used to characterize and test the imager that was designed and fabricated in 0.18um CMOS technology. The imager was tested for capacitance, IV characteristics, EQE, and noise. Table 9 shows a summary of the results.

Table 9 : Summary of Results for CMOS Lateral Imagers

Criteria	Value	
	a-Se	a-Si:H
Storage Capacitance	1.243pF	1.243pF
PPS On Resistance	727Ω	
Max Frame Time	1.3s	57ms
EQE @ 550nm	10%	8.6%
30Hz Contrast Ratio	1.22	1.96
PPS Noise (e-)	700	1280

Chapter 5
Summary and Future Research

This chapter summarizes the thesis citing the applications of high speed x-ray detectors and compromises made to integrate them with CMOS technology along with test results and suggestions for future research.

5.1 Summary

A laterally oriented passive pixel sensor array was designed and fabricated in an industry standard 0.18um CMOS process to gauge the feasibility of integrating large fill factor, high absorption, and lower noise readout than available in competing large area TFT technology.

The chip was tested for functionality based on compromises that had to be made with standard design rules in the conventional process. Two amorphous materials, hydrogenated amorphous silicon and amorphous selenium, were deposited

5.2 Thesis Contributions

This thesis has stepped through the design of a laterally oriented imaging array for medical X-ray imaging. It has shown that a standard 0.18um CMOS process can be interfaced to amorphous semiconductors that allow for high speed circuitry to be combined with high efficiency photodetectors. The final imagers possess lower noise than TFT equivalents and have the capability to integrate electronics underneath the array at an extremely small additional design cost.

Steps and methodology to optimize an imager were developed and utilized in creating the imager. This process will allow for imagers to be created that target different modalities that possess different criteria. These steps also go through issues that can arise when using a standard process to produce a tool not intended for that original process including photoconductor crystallization, step coverage, ESD protection, and sufficient readout electronics to properly characterize the imager.

Finally, test criteria and measurement techniques were setup and employed to characterize the imager. These tests will allow for a standard platform to compare different imagers designs and fabrication techniques in the future.

5.3 Future Recommendations and Research Paths

This project presented itself with various tradeoffs and areas to continue to optimize the area of amorphous semiconductor – CMOS hybrid detectors. The three main areas of potential optimization are the photoconductive layer, the photo-conversion circuit structure, and the readout electronics.

The photoconductive layer in this circuit suffered from high dark currents due to the absence of blocking layers and contamination. Although this was mitigated by the limited lower voltage biases, the reduced field across the photo-conductor resulted in poor EQE which had the effect of diminishing the contrast ratio and frame time of the device. To improve this layer without any major changes it is recommended to decrease the electrode gap on the surface and switching to a high voltage process which allows up to 50V [52] to be collected at C_{pix} before being limited by insulator punch-through about and for the bias applied to be significantly higher per micron of photoconductor, which should result in higher gains for both these materials [23][25]. Also, UWSTAR group members have proposed depositing a unipolar organic blocking layer compatible with an organic photoconductor that is compatible with a large area evaporation process similar to a-Se. This would allow for small dark currents when reverse biased and adequate charge collection in a lateral configuration. As group members get more comfortable with the deposition process as well tighter aspect ratios should be possible and it may be possible to create the advanced lateral pixel architecture seen in Figure 23 with wider electrodes, instead of the combed structure, so that they do not peel off during the annealing stage of the fabrication.

The photo-conversion circuit structure can be improved by implementing more complicated circuitry designed to compensate for large dark currents and to isolate the readout signal from the readout electronics. Such circuits include a switchable APS / PPS structure with correlated double sampling. This prospect of higher vertical integration at the pixel level has already been demonstrated in larger a-Si:H TFT pixels [53] and could provide similar flexibility, speed, and lower noise in a CMOS process.

Finally, the readout electronics can be optimized to be more compatible with the electronics. This may include the vertical integration aspect of the circuit structure, in that charge amplifiers and output buffers can be directly created on the CMOS circuit that simplifies the readout altogether. Also, designing to protect against type of ESD breakdown involves creating diode structures or using the built in ESD structures in the provided 0.18um CMOS process. These were originally overlooked and are capable of being combined with the high voltage CMOS process to create shock resistant bond-pads that result in

less defective dies. By analyzing each node in the circuit ESD structures, such as diode connected FETS, can be placed strategically to create fault tolerant pixels and pixel circuits that allow for handling and processing under less stringent conditions. The difficulty in obtaining reliable and low noise readout electronics should be a prime motivator of future research as it often represents the weakest link in quantum noise limited situations.

References

[1] *On The Physical Lines of Force.* **Maxwell, James Clerk.** London : Philosophical Transactions of the Royal Society of London, 1861, London, Edinburgh, and Dublin Philosophical Magazine and Journal of Science, pp. 1-62.

[2] **Maxwell, James Clerk.** A Dynamic Theory of the Electromagnetic Field. *Philosophical Transactions of the Royal Society of London.* 155, 1864.

[3] *On A New Kind of Rays.* **Röntgen, Wilhelm Conrad.** 274, Würzburg : Nature, 1896, Vol. 53.

[4] *The Early History of X-Ray Diagnosis with Emphasis on the Contributions of Physics 1895 - 1915.* **Mould, R F.** 1995, Surrey : Physics of Medical Biology, 1995, Vol. 40.

[5] *Molecular Structure of Nucleic Acids.* **JD Watson, FHC Crick.** April, London : Nature, 1953, Vol. 4356.

[6] *Techniques in X-Ray Astronomy.* **singh, kulinder pal.** Mumbai : Resonance, 2005, Vol. July.

[7] **Winter, Mark.** WebElements. [Online] 11 15, 2010. [Cited: 11 15, 2010.] www.webelements.com.

[8] **Bushberg.** *The Essential Physics of Medical Imaging.* New York : Lippincott Williams & Wilkins, 2002.

[9] *X-Ray Imaging Physics for Nuclear Medicine Technologists. Part 1: Basic Principles of X-Ray Production.* **Seibert, J Anthony.** 3, Sacramento : Journal for Nuclear Medicine Technology, 2004, Vol. 32.

[10] **Oldnall, Nick.** X-Ray Tube. *XRay200 Nick's Website.* [Online] 10 16, 2010. [Cited: 11 15, 2010.] http://e-radiography.net/.

[11] *A lesion detectability simulation method for digital x-ray imaging.* **V. N. Cooper, J. M. Boone, J. A. Seibert.** 27, Sacramento, California : Medical Physics, 2000, Vols. 0094-2405.

[12] **Carlsson, Carl.** *Imaging Modalities in X-Ray computed tomography and in selected volume tomography.* Linkoping, Sweden : Physics of Medical Biology, 1998. S00.

[13] **Beutel, Jacob.** *Handbook of medical imaging: Physics and psychophysics, Volume 1.* s.l. : Spie Press, 2000.

[14] **James T Dobbins, Devon J Godfrey.** *Digital x-ray tomosynthesis: current state of the art and clinical potential.* Durham, NC : PHYSICS IN MEDICINE AND BIOLOGY, 2003. S0031-9155.

[15] **Krzysztof Iniewski, Dr Karim.** *Medical Imaging: Principles, Detectors, and Electronics.* s.l. : Wiley-Interscience, 2009.

[16] *X-Ray Imaging Physics for Nuclear Medicine Technologists Part 2: X-ray interactions and Image Formation.* **J Anthony Seibert, John Boone.** 1, Sacramento : Journal of Nuclear Medicine Technology, 2005, Vol. 33. 33:3-18.

[17] *Status of Drect Conversion Detectors for Medical Imaging with X-rays.* **M Overdick, C Baumer, KJ Engel, J Fink, C Hermann, H Kruger, M Simon, R Steadman, G Zeitler.** 4, Aachen : IEE Transactions on Nuclear Science, 2009, Vol. 56. 0018-9499.

[18] *Status of Direct Conversion Detectors for Medical Imaging with X-Rays.* **Overdick M, Baumer C, Engel KJ, Fink J, Herrman C, Kruger H, Simon M, Steadman R, Zeitler G.** 4, Aachen : IEE Transactions on Nuclear Science, 2009, Vol. 56. 2025041.

[19] *X-Ray Imaging Performance of Structured Cesium Iodide Scintillators.* **Zhao, Ristic, Rowlands.** 9, New York : Medical Physics, 2004, Vol. 32. 2594.

[20] *Suppression of Afterglow in Microcolumnar CsI:Tl by Codoping With Sm: Recent Advances.* **Nagarkar VV, Thacker SC, Gaysinskiy V, Ovechkina LE, Miller SR, Cool S, Brecher C.** 3, Watertown : IEEE Transactions on Nuclear Sciences, 2009, Vol. 56. 565-570.

[21] **Radiation Monitoring Devices Inc.** *Structured CsI(TI) Scintillators for X-Ray imaging applications.* Watertown : Radiation Monitoring Devices Inc, 2000.

[22] *Multiple doping of CsI:Tl crystals and its effect on afterglow.* **E. E. Ovechkina, a* V. Gaysinskiy,a S. R. Miller,ab C. Brecher,b A. Lempicki,b and V. V. Nagarkara.** 4-5, Watertown : Radiation Monitoring Devices, 2007, Vol. 42.

[23] **S Kasap, J Frey, G Belev, O Tousignant, H Mani, L Laperierre, A Reznik, J Rowlands.** *Amorphous Selenium and its alloys from early xeroradiography to high resolution x-ray image detectors and ultrasensitive imaging tubes.* Saskatoon : Physics Status Solidi, 2009. 10.1002.

[24] *Dependence of DQE of Photoconductive X-Ray detectors on Charge Transport and Trapping.* **Kabir MZ, Kasap SO.** Saskatoon : SPIE, 2002. 3977.

[25] **Mada A, Shaw MP.** *The Physics and applications of amorphous semiconductors.* San Diego : Academic Press Inc, 1988.

[26] *Electronic Structure of Amorphous Semiconductors.* **Robertson, J.** Canada : Advances in Physics, 1983, Vol. 32.

[27] **Ben-Yaacov Ilan, Mishra Umesh.** *Unipolar Space Charge Limited Transport.* Berkeley : University of Southern California, 2004.

[28] **Lucovsky, G.** *Phsyics of selenium and tellurium.* New York : Springer Verlag, 1979.

[29] **Fogal, Bud.** *Electronic Transport Properties of Stabilized Amorphous Selenium X-Ray Photoconductors.* Saskatoon : University of Saskatchewan, 2005.

[30] *Photogeneration of Charge Carriers in Amorphous Selenium.* **JC Knights, EA Davis.** Cambridge : Journal of Physics of Chemical Solids, 1973.

[31] *Onsager mechanism of photogeneration in amorphous selenium.* **Pai DM, Enck RC.** s.l. : Phsyical Review, 1975, Vol. 11.

[32] *Electron and Hole Drift Mobility in Amorphous Silicon.* **Moore, A R.** 11, Princeton : Applied Physics Letters, 1977, Vol. 31.

[33] **Street, RA.** *Hydrogenated Amorphous Silicon.* Cambridge : Cambridge University Press, 1991.

[34] *Optically induced conductivity changes in discharge-produced hydrogenated amorphous silicon.* **Staebler, D. L. and Wronski, C. R.** 6, s.l. : Journal of APplied Phsyics, 1980, Vol. 51.

[35] *Interference free determination of the optical absorption coefficient and the optical gap of amorphous silicon thin films.* **Y Hishikawa, N Nakamura, S Tsuda, S Nakano, Y Kishi, Y Kuwano.** 5, Osaka : Japanese Journal of Applied Physics, 1991, Vol. 30.

[36] *Evaluation of a direct detection selenium-CMOS 8x8 Passive Pixel sensor array for digital x-ray imaging applications.* **Hadji, Bahman.** Waterloo : University of Waterloo, 2009, Vol. Masters Thesis.

[37] *Noise Properties of a a-Se based Flat Panel X-Ray Detector with CMOS Readout Integrated Circuits.* **Adachi Susumu, Hirasawa Shinya, Takahashi Masayuki, Okada Hisao, Yamane Yasukuni, Yamada Satoshi.** Kyoto : Proceedings of SPIE : Physics of Medical Imaging, 2002, Vol. 4682. 1605-7422.

[38] **Wu, Dali.** *Noise Analysis and Measurement for Current Mode and Voltage Mode Active Pixel Sensor Readout Methods.* Waterloo : University of Waterloo, 2009.

[39] **Izadi, Hadi.** Dr. *Personal Communications.* November 26, 2010.

[40] *CMOS Image Sensors : Electronic Camera on a Chip.* **Eric, Fossum.** 10, New Haven : IEE Transactiosn on Electronic Devices, 1997, Vol. 44.

[41] *The Physics of Amorphous-Silicon Thin-Flim Transistors.* **MJ, Powell.** 12, Redhill : IEEE Transactions on Electron Devices, 1989, Vol. 36.

[42] **Jan M. Rabaey, Anantha Chandrakasan, and Borivoje Nikolic´.** *Digital Integrated Circuits.* Berkeley : Prentice-Hall, 2008.

[43] **Paul Siffert (Editor), Eberhard Krimmel (Editor).** *Silicon.* s.l. : Springer, 2004.

[44] **EE Times Asia .** 300-mm wafers drive silicon recovery. *eetimes.com.* [Online] EE Times, 04 27, 2010. [Cited: 06 06, 2010.] http://www.eetimes.com/electronics-news/4088712/300-mm-wafers-drive-silicon-recovery.

[45] **Chapel, Jeff.** What costs most in 300mm? As materials management becomes more complex, FOUP becomes first line of defense. *BNet Business Publications.* [Online] CBS, June 10, 2002. [Cited: Dec 5, 2010.] http://findarticles.com/p/articles/mi_m0EKF/is_24_48/ai_87145967/?tag=content;col1.

[46] *a-Si:H photodiode technology for advanced CMOS active pixel sensor imagers.* **Jeremy A. Theil, Rick Snyder, David Hula, Kirk Lindahl, Homayoon Haddad and Jim Roland.** 2, Santa Clara : Journal of Non-Crystalline Solids, 2002, Vols. 299-302.

[47] **Zvi Or-Bach, eASIC Corp.** Routing density analysis of ASICs, Structured ASICs, and FPGAs. *EE Times Design.* [Online] EE Times, 10 19, 2005. [Cited: 05 05, 2010.] http://www.eetimes.com/design/programmable-logic/4014792/Routing-density-analysis-of-ASICs-Structured-ASICs-and-FPGAs.

[48] **Semenov, Oleg, Sarbishaei, Hossein, Sachdev, Manoj.** *Technologies, ESD Protection Device and Circuit Design for Advanced CMOS.* Waterloo : Springer, 2008. 978-1-4020-8300-6.

[49] *A Review of Electro-static Discharge in Advanced Semiconductor Technology.* **SH, Voldman.** 2004, Essex Junction : Microelectronics Reliability, 2003, Vol. 44.

[50] *A reexamination of silicon avalanche photodiode gain and quantum efficiency.* **McClish, M. Farrell, R. Vanderpuye, K. Shah, K.S.** 23-29, Fajardo : Nuclear Science Symposium Conference Record, 2005 IEEE , 2005 , Vol. 5 .

[51] **Sun Sam Shajing, Saraciftci Niyazi Serdar.** *Organic Photovoltaics.* Baco Raton : CRC Press, 2005.

[52] **MOSIS.** IBM Semiconductor 0.18um 7HV CMOS Process. *The MOSIS Service.* [Online] 12 12, 2010. [Cited: 12 12, 2010.] http://www.mosis.com/ibm/7hv/.

[53] **Izadi, Mohammad Hadi.** *Multimode pixel architectures for large area real time x-ray imaging.* Waterloo : University of Waterloo, 2009.

[54] *CMOS Detector Technology.* **Alan Hoffman, Markus Loose, Vyshnavi Suntharalingam.** 2005, Michigan : Experimental Astronomy, 2006, Vol. 19.